JOURNAL OF COMPUTATIONAL PHYSICS 115, 485–514 (1994)

Extension of the Piecewise Parabolic Method to Multidimensional Ideal Magnetohydrodynamics

WENLONG DAI AND PAUL R. WOODWARD

School of Physics and Astronomy, Supercomputer Institute, Army High Performance Computing Research Center, University of Minnesota, 1100 Washington Avenue South, Minneapolis, Minnesota 55415

Received October 1, 1993; revised July 12, 1994

An extension of the piecewise parabolic method to treat multidimensional ideal magnetohydrodynamical equations is presented in this paper. The multidimensional scheme is constructed from a one-dimensional functioning code based on the dimensional splitting method originally suggested by Strang. The functioning code is built upon a nonlinear Riemann solver for ideal MHD equations recently developed by the authors. The correctness of the scheme is tested in the steepening of waves in both one- and two-dimensional situations and in various MHD shock-tube problems which involve all the discontinuities in ideal MHD. The robust character of the scheme is demonstrated in the shock-tube problems and in the interaction between MHD shocks and a cloud. The results of these problems show that the scheme keeps the principal advantages of a high-order Godunov scheme: robust operation in the presence of very strong waves, thin shock fronts with little attendant noise generation, and thin contact discontinuity. © 1994 Academic Press, Inc.

1. INTRODUCTION

The Godunov's approach [1] of using Riemann problems to obtain robust, upstream centered difference schemes has been proved very effective for compressible gas dynamics. Schemes based on this approach were compared with other techniques in [7] and the special advantages and costs of these schemes were discussed. Since the early MUSCL scheme [2, 3] several other schemes involving higher-order constructions of the Godunov-type with characteristic formulations have been devised (for example, see [4–8]). The principal advantages of these schemes are the robust operation in the presence of very strong waves, thin shock fronts with little attendant noise generation, and thin contact and slip surface discontinuities.

For several years efforts have been underway to develop magnetohydrodynamical (MHD) schemes based upon Godunov's approach and offering the same advantages listed above [9–15]. Especially, Brio and Wu [11] have developed a high-resolution method for MHD based on Roe's approach. Zachary *et al.* [13, 14] have applied a high-order method for general systems of hyperbolic conservation laws to ideal MHD equations, and the high order method for general systems [12] is the extension of Enquist–Osher flux [5]. A major difficulty in developing a high-order Godunov scheme for ideal MHD equations has been the development of a nonlinear Riemann solver and dealing with the nonstrict hyperbolicity of MHD equations [11, 16, 17].

The scheme described here is built upon a nonlinear MHD Riemann solver recently developed by the authors. The procedure for multidimensional MHD simulations is described in this paper. The correctness and robustness of the scheme is demonstrated in various shock-tube problems, in the wave propagation in both one- and two-dimensional simulation domains, and in the interaction between MHD shocks and a cloud.

The plan of this paper is as follows. In the second section the basic equations to be simulated will be given and a Godunov scheme will be introduced. The numerical scheme will be presented in the third section, which includes a nonlinear Riemann solver, a one-dimensional functioning code, our consideration for the nonstrict hyperbolicity, a scheme for multidimensional situations, and discussion of the divergence-free condition of the magnetic field. The numerical examples are in the fourth section, which include the propagation of MHD waves and various shock-tube problems, and the interaction between MHD shocks and a cloud. The conclusions of this paper and brief discussions may be found at the end of this paper.

2. MHD EQUATIONS

The MHD equations characterize the flow of a conducting fluid in the presence of a magnetic field. They represent coupling of the fluid dynamical equations with Maxwell's equations of electrodynamics. By neglecting displacement current, electrostatic force, effects of viscosity, resistivity, and heat conduction, we have the set of ideal MHD equations [18],

$$\frac{\partial \rho}{\partial t} + \nabla \cdot (\rho \mathbf{U}) = 0, \tag{1.1}$$

$$\frac{\partial}{\partial t}(\rho \mathbf{u}) + \nabla \cdot (\rho \mathbf{u}\mathbf{u} + \overleftrightarrow{P}) = 0, \tag{1.2}$$

$$\frac{\partial}{\partial t}(\rho E) + \nabla \cdot (\rho \mathbf{u} E + \overleftrightarrow{P} \cdot \mathbf{u}) = 0, \tag{1.3}$$

0021-9991/94 $6.00

$$\frac{\partial \mathbf{B}}{\partial t} + \nabla \cdot \overleftrightarrow{T} = 0, \tag{1.4}$$

where ρ is the mass density, $\mathbf{u}$ is the flow velocity, $\mathbf{B}$ is the magnetic field, $\overleftrightarrow{P}$ is the stress tensor including the effects of the magnetic fields as well as the thermal pressure p, E is the total specific energy, and $\overleftrightarrow{T}$ is the antisymmetric tensor product of the flow velocity and the magnetic field,

$$P_{imj} \equiv (p + \frac{1}{8\pi}\mathbf{B}^2)\delta_{ij} - \frac{1}{4\pi}B_iB_j,$$

$$E \equiv \varepsilon + \frac{1}{2}\mathbf{u}^2 + \frac{1}{8\pi\rho}\mathbf{B}^2,$$

$$T_{ij} \equiv u_iB_j - u_jB_i$$

with ε being the specific internal energy. It is easy to see that $\nabla \cdot \overleftrightarrow{T}$ is $\nabla \times (\mathbf{u} \times \mathbf{B})$. Writing it in the form above shows more clearly that the equation is in the conservation form. This set of equations has to be completed with an equation of state. The thermal pressure is assumed to be related to the internal energy density ε through the gamma-law $p = (\gamma - 1)\rho\varepsilon$ with γ as the ratio of the specific heat capacities of the gas.

Since we will be working on a Lagrangian mass coordinate $\mathbf{m}$, which is defined by $d\mathbf{m} = d\mathbf{r}$ with $\mathbf{r} \equiv (x, y, z)$, we rewrite the ideal MHD equations in the Langrangian mass coordinate:

$$\frac{dV}{dt} - \nabla_m \cdot \mathbf{u} = 0, \tag{2.1}$$

$$\frac{d\mathbf{u}}{dt} + \nabla_m \cdot \overleftrightarrow{P} = 0, \tag{2.2}$$

$$\frac{dE}{dt} + \nabla_m \cdot (\mathbf{u} \cdot \overleftrightarrow{P}) = 0, \tag{2.3}$$

$$\frac{d(V\mathbf{B})}{dt} - \nabla_m \cdot (\mathbf{Bu}) = 0, \tag{2.4}$$

where V is the specific volume $V \equiv 1/\rho$.

In this paper we will construct a high-order numerical scheme which employs the dimensional splitting technique. Therefore we write a projection (e.g., on the x-direction) of the ideal MHD equations explicitly:

$$\frac{\partial \mathbf{U}}{\partial t} + \frac{\partial \mathbf{F}(\mathbf{U})}{\partial m} = 0 \tag{3a}$$

and

$$\frac{\partial}{\partial t}(VB_x) - \frac{\partial}{\partial m}(B_xu_x) = 0, \tag{3b}$$

with

$$\mathbf{U} \equiv \begin{bmatrix} V \\ u_x \\ u_y \\ u_z \\ VB_y \\ VB_z \\ E \end{bmatrix}, \quad \mathbf{F}(\mathbf{U}) \equiv \begin{bmatrix} -u_x \\ P \\ \Lambda_y \\ \Lambda_z \\ -B_xu_y \\ -B_xu_z \\ Pu_x + \Lambda_yu_y + \Lambda_zu_z \end{bmatrix}. \tag{4}$$

Here the mass coordinate is defined by $dm \equiv \rho dx$ as in [7, 8]; P, Λ_y, and Λ_z are the diagonal and off-diagonal elements of the tensor $\overleftrightarrow{P}$:

$$P \equiv p + \frac{1}{8\pi}(B_y^2 + B_z^2 - B_x^2),$$

$$\lambda_y \equiv -\frac{1}{4\pi}B_xB_y,$$

$$\Lambda_z \equiv -\frac{1}{4\pi}B_xB_z.$$

Here we have written Eq. (3b) separately, since our one-dimensional functioning code, which is used in our multidimensional scheme and will be introduced in Section 3.2, deals with only Eq. (3a).

Considering a zone in a Langrangian grid with its left and right interfaces x_L and x_R, respectively, we write the following difference scheme for the conservation law Eq. (3):

$$\langle \mathbf{U}(\Delta t) \rangle = \langle \mathbf{U}(0) \rangle + \frac{\Delta t}{\Delta m}(\overline{\mathbf{F}}_L - \overline{\mathbf{F}}_R). \tag{5}$$

Here Δt is the time step and Δm is the mass contained in the zone, $\langle \mathbf{U}(t) \rangle$ is the average of $\mathbf{U}$ over the zone at time t, and $\overline{\mathbf{F}}_L$ (or $\overline{\mathbf{F}}_R$) is the time-averaged flux at the left (or right) interface of the zone during the time step Δt; i.e.,

$$\langle \mathbf{U}(t) \rangle \equiv \frac{1}{\Delta x}\int_{\Delta x} \mathbf{U}(t, x)dx,$$

$$\overline{\mathbf{F}}_{L,R} \equiv \frac{1}{\Delta t}\int_{\Delta t} \mathbf{U}(t, x_{L,R})dt$$

with Δx the width of the zone. This discretized Equation (5) may be obtained by integrating Eq. (3), over the rectangular $x_L < x < x_R$ and $0 < t < \Delta t$ in the $(x - t)$ space. The discretized form of Eq. (5) is exact if the time-averaged flux $\overline{\mathbf{F}}_{L,R}$ may be found exactly. Our nonlinear Riemann solver will be used to calculate the set of time-averaged flux.

3. NUMERICAL SCHEME

In this section, we will introduce a high-order numerical scheme for the ideal MHD equations (1.1)–(1.4), which includes a nonlinear Riemann solver, a one-dimensional functioning code, the consideration of the nonstrict hyperbolicity, the scheme for multidimensional situations, and the discussion for the divergence-free condition for the magnetic field. Before we discuss the nonstrict hyperbolicity, we assume that any component of the magnetic field does not vanish exactly.

3.1. A Nonlinear Riemann Solver

A Riemann problem in ideal MHD is an initial value problem, Eq. (3), subject to a specific initial condition:

$$\mathbf{U}_0(x) = \begin{cases} \mathbf{U}_L & (x < 0), \\ \mathbf{U}_R & (x > 0). \end{cases}$$

Here $\mathbf{U}_L$ and $\mathbf{U}_R$ are any given left and right states. The difficulty in the Riemann problem is the more than one discontinuities which may be generated from the initial conditions. As we know, across any discontinuity in ideal MHD, the longitudinal component of the magnetic field remains unchanged. Therefore we assume that the component is a constant in this subsection. The case with a varying longitudinal component, which will be encountered in a dimensional splitting method, will be discussed in the subsection entitled "A Scheme for Multidmensional Situations."

It is well known that the basic equation (3) allows three kinds of waves: fast, Alfven, and slow waves, besides entropy waves. An entropy wave is stationary in a Langrangian coordinate, and the fast, slow, and Alfven waves have their wave speeds C_f, C_a, and C_s, respectively:

$$C_{f,s}^2 = \frac{1}{2}[(C_0^2 + C_a^2 + C_t^2) \pm \sqrt{(C_0^2 + C_a^2 + C_t^2)^2 - 4C_0^2C_a^2}].$$

Here the plus sign is for fast waves, and the minus sign for slow waves. C_0, C_a, and C_t are defined as

$$C_0 \equiv \sqrt{\gamma p \rho},$$
$$C_a \equiv \sqrt{\rho B_x^2/(4\pi)},$$
$$C_t \equiv \sqrt{\rho(B_y^2 + B_z^2)/(4\pi)}.$$

Note that the wave speeds are defined in the Langrangian mass coordinate. Their equivalences in an Eulerian coordinate may be obtained through dividing them by the mass density ρ. Since smooth fast and slow waves may develop into shocks, our nonlinear Riemann solver is based on jump conditions for discontinuities. Such jump conditions may be derived directly from the conservations of the mass, momentum, energy, and magnetic flux. An example of such derivation may be found in the book by Courant and Friedrichs [19]. The jump conditions may also be obtained simply by integrating Eq. (3) over a discontinuity:

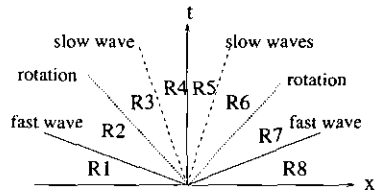

FIG. 1. All possible waves generated from a MHD Riemann problem and eight possibly different states divided by the wave fronts.

$$W[V] = -[u_x], \tag{6.1}$$
$$W[u_x] = [P], \tag{6.2}$$
$$W[u_y] = [\Lambda_y], \tag{6.3}$$
$$W[u_z] = [\Lambda_z], \tag{6.4}$$
$$W[VB_y] = -B_x[u_y], \tag{6.5}$$
$$W[VB_z] = -B_x[u_z], \tag{6.6}$$
$$W[E] = [u_xP] + [u_y\Lambda_y] + [u_z\Lambda_z]. \tag{6.7}$$

Here W is the speed of the discontinuity surface propagating in the mass coordinate. The bracket $[X]$ stands for the difference between the states on the two sides of the surface, i.e., $[X] = X_1 - X_0$. Physically, W is the mass flux across the discontinuity, i.e., $W = (s - u_{x0})\rho_0$ with s being a usual shock speed and u_{x0} being the x-component of the flow velocity in the preshock state. W is negative when the discontinuity propagates in the negative x-direction. This set of jump conditions is equivalent to that derived from the Eulerian equations in the book by Landau and Lifshitz [18]. In our Riemann solver, we will approximate rarefaction waves by rarefaction shocks obeying the jump conditions given above (and involving decreases in the entropy).

There are five kinds of discontinuities which may exist under ideal MHD equations: contact discontinuities, tangential discontinuities, fast shocks, slow shocks, and rotational discontinuities. A more detailed description of MHD discontinuities may be found in many standard texts (for example, Landau and Lifshits [18], Jeffrey and Taniuti [20], Kulikovskiy and Lyubimov [21], Kantrowitz and Petschek [22]).

In a general MHD Riemann problem, there are six waves traveling leftward and rightward, which may be generated from an initial discontinuity. The waves traveling leftward are separated by a contact surface from the waves traveling rightward. Each wave may be either continuous or discontinuous. The appearance and the strength of each wave depends on specific data in the initial discontinuity. The wave fronts corresponding

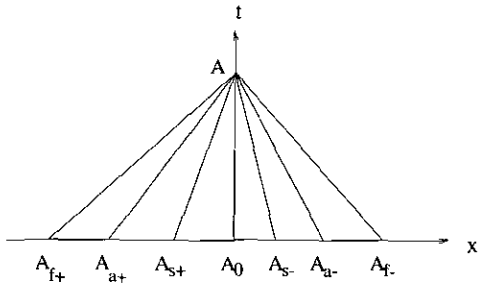

FIG. 2. Illustrations for domains of dependence for various waves.

to the three waves in either direction and a contact surface separate whole $(x - t)$ plane into eight possibly different regions. We label them R1, R2, R3, R4, R5, R6, R7, and R8, respectively, as shown in Fig. 1. The states in the regions R1 and R8 are the left and right states in the Riemann problem, respectively.

To find a nonlinear Riemann solver, we find a formula for the shock speeds, W_f for fast shocks and W_s for slow shocks, in terms of the preshock state and one transverse component of the magnetic field in the postshock state:

$$W_{f,s}^2 = \frac{1}{2(1+A_0)}\{(C_s^2 + C_f^2 + A_1) \pm \sqrt{(C_s^2 + C_f^2 + A_1)^2 - 4(1+A_0)(C_s^2 C_f^2 - A_2)}\}. \tag{7}$$

Here the plus sign is for fast shocks and the minus sign for slow shocks. $A_{0,1,2}$ are defined as

$$A_0 \equiv -\frac{1}{2}(\gamma - 1)\frac{[\Lambda_y]}{\Lambda_y},$$

$$A_1 \equiv \frac{1}{2}\{(\gamma - 2)\lambda\rho\frac{B_y}{B_x}[\Lambda_y] + 2C_0^2 - (\gamma - 4)C_t^2 - 2\gamma C_a^2\}\frac{[\Lambda_y]}{\Lambda_y},$$

$$A_2 \equiv \frac{1}{2}\{\lambda\rho^2[\Lambda_y]^2 + (\gamma + 2)\lambda\rho^2\Lambda_y[\Lambda_y] + (\gamma + 1)C_a^2C_t^2 + (\gamma + 1)C_a^4 - 2C_0^2C_a^2\}\frac{[\Lambda_y]}{\Lambda_y}.$$

Here $\lambda \equiv 1 + (B_z/B_y)^2$ and the variables in $A_{0,1,2}$ are evaluated at the preshock state except for the jump $[\Lambda_y]$. For a given set of left and right states, we construct a Riemann solution by the following procedures:

(1) Guess one transverse component (e.g., y-component) B_{y2}, B_{y4}, and B_{y7} of the magnetic field in regions R2, R4, and R7, and the orientation ψ of the transverse part of the magnetic field in regions R3, R4, R5, and R6. Here $\tan\psi \equiv B_{z3}/B_{y3}$.

(2) Consider the right and left states as two preshock states, calculate two fast shock speeds using Eq. (7), one for the wave traveling rightward and the other for the wave traveling leftward, then from the jump conditions (6.1)–(6.7) with these two shock speeds and the values of B_y in the two postshock states, find the complete states in regions R2 and R7, respectively.

(3) Perform the rotations with the earlier guess ψ, then use the jump conditions (6.1)–(6.7) with the speed W equal to the Alfven speeds in regions R2 and R7 to get the complete states in regions R3 and R6, respectively.

(4) Consider the states in regions R3 and R6 as two preshock states, repeat step (2) for two slow shocks instead of fast shocks to get the states in regions R4 and R5.

(5) Apply the conditions for a contact discontinuity between regions R4 and R5 to improve the earlier guess on B_{y2}, B_{y4}, B_{y7}, and ψ as described below. With this improved guess, go back to the procedure (1).

Following the first four steps, the state in region R4 (or R5) is a function of B_{y2}, B_{y4}, ψ (or B_{y2}, B_{y4}, B_{y7}, ψ). If B_{y2}, B_{y4}, B_{y7}, and ψ are the solutions of the Riemann problem, two states in regions R4 and R5 should be the same except for their mass densities and total energies. The remaining requirements for a contact discontinuity may be expressed as the same (p, u_x, u_y, u_z) in regions R4 and R5:

$$u_{x4}(B_{y2}, B_{y4}, \psi) = u_{x5}(B_{y7}, B_{y4}, \psi),$$

$$u_{y4}(B_{y2}, B_{y4}, \psi) = u_{y5}(B_{y7}, B_{y4}, \psi),$$

$$u_{z4}(B_{y2}, B_{y4}, \psi) = u_{z5}(B_{y7}, B_{y4}, \psi),$$

$$p_4(B_{y2}, B_{y4}, \psi) = p_5(B_{y7}, B_{y4}, \psi),$$

This set of equations can be solved for B_{y2}, B_{y4}, B_{y7}, and ψ iteratively by the Newton's method, i.e., the modifications δB_{y2}, δB_{y4}, δB_{y7}, and $\delta\psi$ of the initial guess on B_{y2}, B_{y4}, B_{y4}, B_{y7}, and ψ may be found by the following set of equations:

$$\frac{\partial u_{x4}}{\partial B_{y2}}\delta B_{y2} + \left(\frac{\partial u_{x4}}{\partial B_{y4}} - \frac{\partial u_{x5}}{\partial B_{y4}}\right)\delta B_{y4} - \frac{\partial u_{x5}}{\partial B_{y7}}\delta B_{y7} + \left(\frac{\partial u_{x4}}{\partial \psi} - \frac{\partial u_{x5}}{\partial \psi}\right)\delta\psi = u_{x5} - u_{x4},$$

$$\frac{\partial u_{y4}}{\partial B_{y2}}\delta B_{y2} + \left(\frac{\partial u_{y4}}{\partial B_{y4}} - \frac{\partial u_{y5}}{\partial B_{y4}}\right)\delta B_{y4} - \frac{\partial u_{y5}}{\partial B_{y7}} + \left(\frac{\partial u_{y4}}{\partial \psi} - \frac{\partial u_{y5}}{\partial \psi}\right)\delta\psi = u_{y5} - u_{y4},$$

$$\frac{\partial u_{z4}}{\partial B_{y2}}\delta B_{y2} + \left(\frac{\partial u_{z4}}{\partial B_{y4}} - \frac{\partial u_{z5}}{\partial B_{y4}}\right)\delta B_{y4} - \frac{\partial u_{z5}}{\partial B_{y7}}\delta B_{y7} + \left(\frac{\partial u_{z4}}{\partial \psi} - \frac{\partial u_{z5}}{\partial \psi}\right)\delta\psi = u_{z5} - u_{z4},$$

$$\frac{\partial p_4}{\partial B_{y2}}\delta B_{y2} + \left(\frac{\partial p_4}{\partial B_{y4}} - \frac{\partial p_5}{\partial B_{y4}}\right)\delta B_{y4} - \frac{\partial p_5}{\partial B_{y7}}\delta B_{y7} + \left(\frac{\partial p_4}{\partial \psi} - \frac{\partial p_5}{\partial \psi}\right)\delta\psi = p_5 - p_4.$$

The initial guess needed in the nonlinear Riemann solver may be obtained from a linear Riemann solver. Our linear Riemann solver is based on characteristic formulations. Characteristic formulations in ideal MHD equations have also been discussed by previous investigators (e.g., [9–11, 13, 14]).

Following the general outline given by Courant and Friedrichs [19], it is not difficult to find all the characteristic curves and their associated Riemann invariants. The first characteristic curve is a straight line, which is found to be

$$L_0: \frac{dx}{dt} = 0,$$

and its associated Riemann invariant is

$$R_0 = pV^\gamma. \tag{8.1}$$

The logarithm of this invariant is proportional to the specific entropy. Along the characteristic curve L_0, the entropy is constant, but across it, the specific volume and entropy may have jumps. The remaining six Riemann invariants for two fast, two slow, and two Alfven waves may be expressed only as inexact differentials:

$$dR_{f\pm} \equiv (C_f^2 - C_a^2)(dP \pm C_f du_x) + \rho\Lambda_y(d\Lambda_y \pm C_f du_y) + \rho\Lambda_z(d\Lambda_z + C_f du_z), \tag{8.2}$$

$$dR_{s\pm} \equiv (C_s^2 - C_a^2)(dP \pm C_s du_x) + \rho\Lambda_y(d\Lambda_y \pm C_s du_y) + \rho\Lambda_z(d\Lambda_z + C_s du_z), \tag{8.3}$$

$$dR_{a\pm} \equiv \pm C_a(B_z du_y - B_y du_z) + (B_z d\Lambda_y - B_y d\Lambda_z). \tag{8.4}$$

Along any characteristic curve, L, which is defined as $dx/dt = C$ with C being among $C_{f\pm}$, $C_{a\pm}$, $C_{s\pm}$, its associated Riemann invariant R remains unchanged, i.e.,

$$\frac{dR}{dt} + C\frac{\partial R}{\partial x} = 0.$$

Only for the initial guess do we assume that the difference between left and right states is small. The initial solution for $(P, u_x, u_y, u_z, \Lambda_y, \Lambda_z)$ in region R4 may be obtained from the conservation of the Riemann invariants along their characteristic curves:

$$a_f(P - P_L) + a_f C_f(u_x - u_{xL}) + \rho\Lambda_y(\Lambda_y - \Lambda_{yL}) + \rho\Lambda_y C_f(u_y - u_{yL}) + \rho\Lambda_z(\Lambda_z - \Lambda_{zL}) + \rho\Lambda_z C_f(u_z - u_{zL}) = 0, \tag{9.1}$$

$$a_f(P - P_R) + a_f C_f(u_x - u_{xR}) + \rho\Lambda_y(\Lambda_y - \Lambda_{yR}) - \rho\Lambda_y C_f(u_y - u_{yR}) + \rho\Lambda_z(\Lambda_z - \Lambda_{zR}) - \rho\Lambda_z C_f(u_z - u_{zR}) = 0, \tag{9.2}$$

$$a_s(P - P_L) + a_s C_s(u_x - u_{xL}) + \rho\Lambda_y(\Lambda_y - \Lambda_{yL}) + \rho\Lambda_y C_s(u_y - u_{yL}) + \rho\Lambda_z(\Lambda_z - \Lambda_{zL}) + \rho\Lambda_z C_s(u_z - u_{zL}) = 0, \tag{9.3}$$

$$a_s(P - P_R) - a_s C_f(u_x - u_{xR}) + \rho\Lambda_y(\Lambda_y - \Lambda_{yR}) - \rho\Lambda_y C_s(u_y - u_{yR}) + \rho\Lambda_z(\Lambda_z - \Lambda_{zR}) - \rho\Lambda_z C_s(u_z - u_{zR}) = 0, \tag{9.4}$$

$$C_a B_z(u_y - u_{yL}) - C_a B_y(u_z - u_{zL}) + B_z(\Lambda_y - \Lambda_{yL}) - B_y(\Lambda_z - \Lambda_{zL}) = 0, \tag{9.5}$$

$$-C_a B_z(u_y - u_{yR}) + C_a B_y(u_z - u_{zR}) + B_z(\Lambda_y - \Lambda_{yR}) - B_y(\Lambda_z - \Lambda_{zR}) = 0. \tag{9.6}$$

Here the subscript $_L$ (or $_R$) refers to the evaluation at the left (or right) state, and the coefficients $a_{f,s}$ are defined as $a_{f,s} \equiv (C_{f,s}^2 - C_a^2)$. All the coefficients in Eqs. (9.1)–(9.5) may be evaluated at either the left or the right state under the linear approximation.

Our nonlinear Riemann solver is able to give enough accurate solutions through a sufficient number of iterations, but for most problems in simulations, one or two iterations is enough to get a sufficiently accurate flux. Table VIIa shows the solutions for a Riemann problem in our formulations after five iterations, which contain two fast rarefaction waves, two slow shocks with Mach numbers 1.05 and 2.2, respectively, one rotational and one contact discontinuity. Table VIIb shows the convergence of wave speeds $W_{f\pm}$ for the two fast rarefaction waves and $W_{s\pm}$ for the two slow shocks.

In case our nonlinear Riemann solver failed at a specific interface and a specific time in a simulation, we simply use the solution from our linear Riemann solver in our numerical code. Several other strategies (e.g., the use of averages between the left and right states) have been tested in all the numerical examples in this paper; we did not find any noticeable difference.

3.2. One-Dimensional Functioning Code

Our one-dimensional functioning code is used to update physical variables in a one-dimensional pass (for example, an x-pass equation (3a)) and the procedures in the code will be

used in our multidimensional scheme. The functioning code starts from zone-averages of a set of physical variables (ρ, p, u_x, u_y, u_z, B_x, B_y, B_z) and updates the set of variables except B_x through solving Eq. (3a). The longitudinal component B_x is allowed to vary with the space coordinate x in the functioning code. The differentials of Riemann invariants, Eqs. (10.2)–(10.4), are first derived from this set of physical variables. Then a cubic polynomial is used to interpolate each of the differentials and find the values of the Riemann invariant at the interfaces of computational zones. Except for the mass density ρ and the field component B_x, the values of other physical variables at the interfaces are obtained through these interpolated Riemann invariants. For example, from the values $R_{f\pm,L}$, $R_{s\pm,L}$, and $R_{a\pm,L}$ of Riemann invariants at the left interface of a zone, we find the values P, Λ_y, Λ_z, u_x, u_y, and u_z at the left interface through the following set of equations:

$$
\begin{aligned}
&a_f(P - \langle P\rangle) + a_f C_f(u_x - \langle u_x\rangle) + \rho\Lambda_y(\Lambda_y - \langle\Lambda_y\rangle)\\
&\quad + \rho\Lambda_y C_f(u_y - \langle u_y\rangle) + \rho\Lambda_z(\Lambda_z - \langle\Lambda_z\rangle)\\
&\quad + \rho\Lambda_z C_f(u_z - \langle u_z\rangle) = R_{f+,L},\\
&a_f(P - \langle P\rangle) - a_f C_f(u_x - \langle u_x\rangle) + \rho\Lambda_y(\Lambda_y - \langle\Lambda_y\rangle)\\
&\quad - \rho\Lambda_y C_f(u_y - \langle u_y\rangle) + \rho\Lambda_z(\Lambda_z - \langle\Lambda_z\rangle)\\
&\quad - \rho\Lambda_z C_f(u_z - \langle u_z\rangle) = R_{f-,L},\\
&a_s(P - \langle P\rangle) + a_s C_s(u_x - \langle u_x\rangle) + \rho\Lambda_y(\Lambda_y - \langle\Lambda_y\rangle)\\
&\quad + \rho\Lambda_y C_s(u_y - \langle u_y\rangle) + \rho\Lambda_z(\Lambda_z - \langle\Lambda_z\rangle)\\
&\quad + \rho\Lambda_z C_s(u_z - \langle u_z\rangle) = R_{s+,L},\\
&a_s(P - \langle P\rangle) + a_s C_f(u_x - \langle u_x\rangle) + \rho\Lambda_y(\Lambda_y - \langle\Lambda_y\rangle)\\
&\quad - \rho\Lambda_y C_s(u_y - \langle u_y\rangle) + \rho\Lambda_z(\Lambda_z - \langle\Lambda_z\rangle)\\
&\quad - \rho\Lambda_z C_s(u_z - \langle u_z\rangle) = R_{s-,L},\\
&C_a B_z(u_y - \langle u_y\rangle) - C_a B_y(u_z - \langle u_z\rangle) + B_z(\Lambda_y - \langle\Lambda_y\rangle)\\
&\quad - B_y(\Lambda_z - \langle\Lambda_z\rangle) = R_{a+,L},\\
&-C_a B_z(u_y - \langle u_y\rangle) + C_a B_y(u_z - \langle u_z\rangle) + B_z(\Lambda_y - \langle\Lambda_y\rangle)\\
&\quad - B_y(\Lambda_z - \langle\Lambda_z\rangle) = R_{a-,L}.
\end{aligned}
$$

Here $\langle\ \ \rangle$ stands for a zone-average, and all the coefficients are evaluated at the zone-averages. We should mention that a simpler way is to interpolate physical variables directly to find their values at the interfaces of zones, and it takes less computation and may achieve equally good results for most shock problems. In his numerical experiments for gas dynamics, Woodward has realized [23] that interpolating Riemann invariants instead of physics variables may reduce noise generation for slowly moving shocks. Therefore, the numerical examples in this paper are calculated through the interpolation of Riemann invariants. All the examples in this paper are also calculated through the interpolation of the normal physical variables, and we did not find noticeable differences in the results, except for the first example. When we introduce the first example in Fig. 3 for the steepening of a MHD wave in the next section, we will point out the difference in results between the two kinds of interpolation.

After we get the values of the normal physical variables at the interfaces, the monotonicity constraint originally suggested by Van Leer [2] is applied to these values at the interfaces. As we know, interpolated structures are not always monotonically increasing (decreasing) even though they have been constructed from monotone data. The over- and undershoots in the interpolated internal zone structures eventually give rise to over- and undershoots in the zone-averaged data. Van Leer realized that an advection scheme may be made to preserve the monotonicity of its initial data if any nonmonotone interpolated zone structures are flattened so that they become monotone. This leads the Van Leer's monotonicity constraint: no values interpolated within a zone shall lie outside the range defined by the zone averages for this zone and its two neighbors. The difference in the results between with and without the monotonicity constraint may be found in [24].

We assume that the flow is continuous inside each zone but it may have big jumps across an interface of two neighboring zones. After the monotonicity constraint is applied, a parabola defined by a zone-average and the values at two edges of the zone is used to interpolate the structure inside a zone for the calculation of a domain-average which is the average over a domain of dependence. Consider a point A at an interface as shown in Fig. 2 and draw six characteristic curves through the point A, which are approximated by six straight lines. The sections $A_{f+}A_0$, $A_{a+}A_0$, and $A_{s+}A_0$ are the domains of dependence for the fast, Alfven, and slow waves traveling rightward, respectively, and the sections $A_{f-}A_0$, $A_{a-}A_0$, and $A_{s-}A_0$ are the domains of dependence for the fast, Alfven, and slow waves traveling leftward, respectively. The extension of each domain of dependence for waves traveling rightward is approximately equal to $C_L\Delta t$, and the extension of each domain of dependence for a wave traveling leftward is approximately $C_R\Delta t$, where C is an associated wave speed among C_f, C_a, and C_s and the subscript $_L$ (or $_R$) refers to the evaluation at the average over the left (or right) zone of the interface. The domain-average on each of the domains may be found through the interpolated internal zone structure. Effective left and right states for a Riemann problem arising from an interface between $(i-1)$th and ith zones are found through two sets of Riemann invariants at two sides of the interface, respectively. For example, the effective left states (P, Λ_y, Λ_z, u_x, u_y, u_z) are found through the following set of equations which come from the conservation of Riemann invariants:

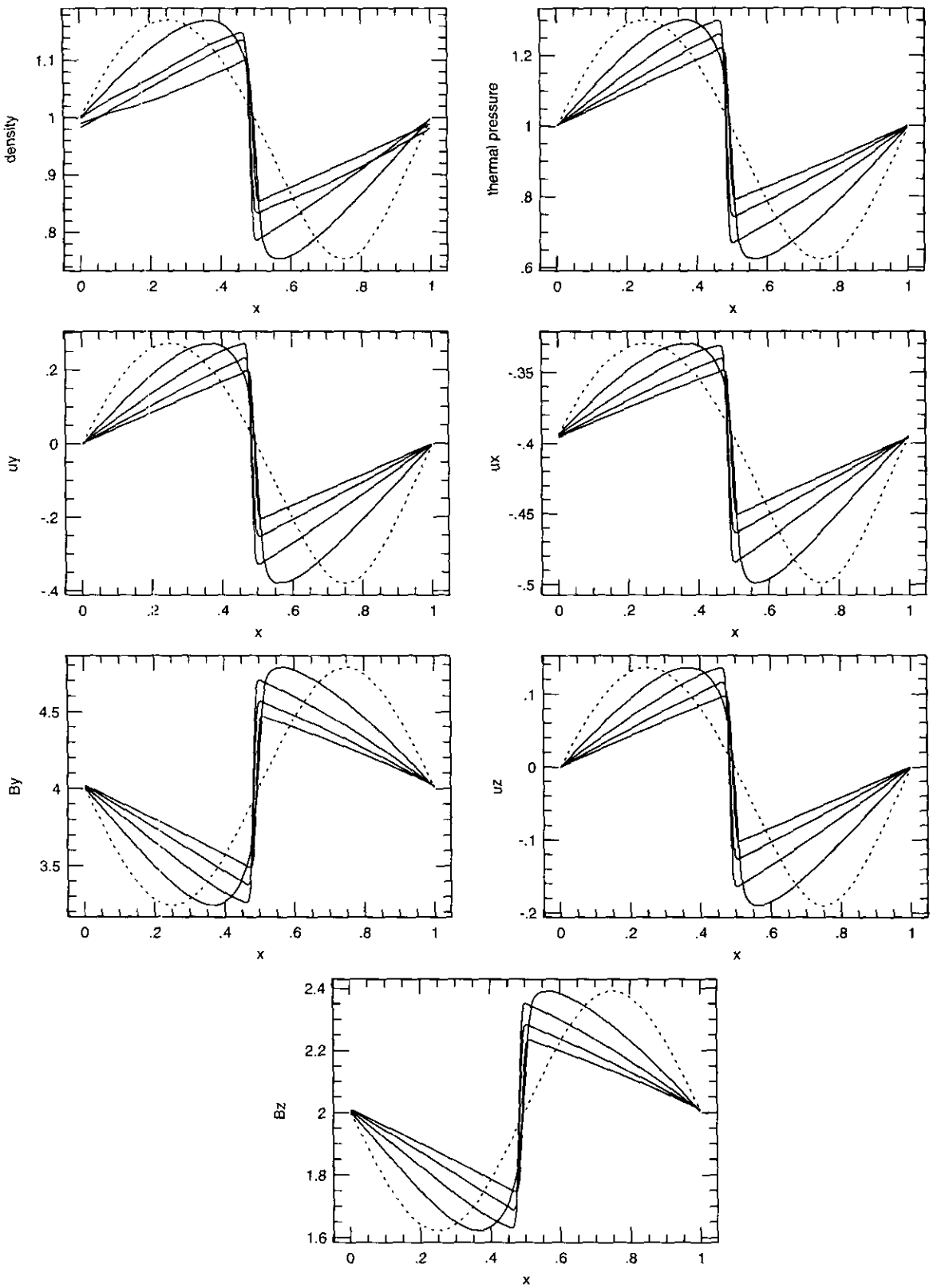

FIG. 3. The steepening of a MHD slow wave: $\gamma = \frac{5}{3}$, $B_x = 2$. Dashed lines are initial conditions and the solid lines are the profiles at four instants $t =$ 1.27, 2.54, 3.82, and 5.08. During each interval the wave traveled about a half wavelength.

$$a_f(P - \langle P\rangle_{df}) + a_f C_f(u_x - \langle u_x\rangle_{df}) + \rho\Lambda_y(\Lambda_y - \langle\Lambda_y\rangle_{df}) + \rho\Lambda_y C_f(u_y - \langle u_y\rangle_{df}) + \rho\Lambda_z(\Lambda_z - \langle\Lambda_z\rangle_{df}) + \rho\Lambda_z C_f(u_z - \langle u_z\rangle_{df}) = 0, \quad (10.1)$$

$$a_s(P - \langle P\rangle_{ds}) + a_s C_s(u_x - \langle u_x\rangle_{ds}) + \rho\Lambda_y(\Lambda_y - \langle\Lambda_y\rangle_{ds}) - \rho\Lambda_y C_s(u_y - \langle u_y\rangle_{ds}) + \rho\Lambda_z(\Lambda_z - \langle\Lambda_z\rangle_{ds}) + \rho\Lambda_z C_s(u_z - \langle u_z\rangle_{ds}) = 0, \quad (10.2)$$

$$C_a B_z(u_y - \langle u_y\rangle_{da}) - C_a B_y(u_z - \langle u_z\rangle_{da}) + B_z(\Lambda_y - \langle\Lambda_y\rangle_{da}) - B_y(\Lambda_z - \langle\Lambda_z\rangle_{da}) = 0, \quad (10.3)$$

$$a_f(P - P_{(i-1)R}) - a_f C_f(u_x - u_{x(i-1)R}) + \rho\Lambda_y(\Lambda_y - \Lambda_{y(i-1)R}) - \rho\Lambda_y C_f(u_y - u_{y(i-1)R}) + \rho\Lambda_z(\Lambda_z - \Lambda_{z(i-1)R}) - \rho\Lambda_z C_f(u_z - u_{z(i-1)R}) = 0, \quad (10.4)$$

$$a_s(P - P_{(i-1)R}) - a_s C_f(u_x - u_{x(i-1)R}) + \rho\Lambda_y(\Lambda_y - \Lambda_{y(i-1)R}) - \rho\Lambda_y C_s(u_y - u_{y(i-1)R}) + \rho\Lambda_z(\Lambda_z - \Lambda_{z(i-1)R}) - \rho\Lambda_z C_s(u_z - u_{z(i-1)R}) = 0, \quad (10.5)$$

$$-C_a B_z(u_y - u_{y(i-1)R}) + C_a B_y(u_z - u_{y(i-1)R}) + B_z(\Lambda_y - \Lambda_{y(i-1)R}) - B_y(\Lambda_z - \Lambda_{z(i-1)R}) = 0. \quad (10.6)$$

Here the subscripts $_{df}$ (or $_{ds}$ or $_{da}$) stand for the average on the domain of dependence for fast (or slow or Alfven) waves in the $(i-1)$th zone, and the subscript $_{(i-1)R}$ stands for the value at the right edge of the $(i-1)$th zone. The coefficients in this set of equations are evaluated at the zone-averages on the $(i-1)$th zone. Similar equations may be used to find the effective right state if we replace the domain-averages in Eqs. (10.1)–(10.3) by the values at the left edge of the ith zone and replace subscript $_{(i-1)R}$ by $\langle\ \ \rangle_{fd}$ in Eq. (10.4), $_{(i-1)R}$ by $\langle\ \ \rangle_{sd}$ in Eq. (10.4), $_{(i-1)R}$ by $\langle\ \ \rangle_{ad}$ in Eq. (10.6), and if the coefficients are evaluated at the zone averages over the ith zone. Since we assume that the flow inside each zone is continuous, we may use the characteristic formulations to find the effective left and right states.

After we found the effective left and right states, we use the nonlinear Riemann solver described in Section 3.1 to find the set of flux needed in the Godunov scheme, Eq. (5), and update the conserved quantities, i.e., mass, momentum, energy, and magnetic flux, by adding the flux advected into and subtracting the flux advected out from a zone. Thus we have completed one dynamical step in the Lagrangian grid.

One widely used formulation of Eulerian hydrodynamics algorithms, due originally to DeBar [27], is that of performing a hydrodynamics calculation for a one time step using a Lagrangian method and mapping the results onto a fixed Eulerian grid. After zone-averages in the Langrangian grid are obtained, a cubic polynomial is used to interpolate the zone-averages in order to find the values at edges of zones for each of physical variable. Then the monotonicity constraint described above is used to adjust the values at the edges. A parabola defined by a zone-average and the values at the two edges of the zone is used for the internal zone structure for each physical variable in order to peform the mapping. The mapping procedure is only a transformation from one grid to the other, and keeps the conservation of the mass, momentum, energy, and magnetic flux.

Finally, an artificial viscosity is used in our code for strong shocks as in the piecewise parabolic method (PPM) scheme. Attendant noise will be probably generated if no artificial viscosity is introduced. For the artificial viscosity, the code first finds the locations of strong shocks by checking the jump in total pressure P and the divergence of the flow velocity. After estimating the wave speed for the noise traveling away from the shock in the shock frame and the domain of diffusion, the code performs the diffusion by exchanging the amounts of the mass, momentum, energy, and magnetic flux contained in the two diffusion regions at two sides of an interface if there is a strong shock present there. A more detailed discussion about the artificial viscosity may be found in [7, 24]. The technique introduced there for PPM is used in the scheme presented in this paper. We mention that the code is still stable even if we turn off the artificial viscosity for a strong shock. The results when we turn off the artificial viscosity will be mentioned for the propagation of a strong shock in Figs. 4a,b.

We should mention that in the one-dimensional functioning code only two transverse components of the magnetic field are updated, while the longitudinal component B_x remains unchanged. The component B_x will be updated in other passes in our multidimensional scheme.

3.3. Consideration of the Nonstrict Hyperbolicity

Mathematically, the vanishing of the longitudinal or tangential component of a local magnetic field will cause a singularity because of the vanishing expansion coefficients when the Riemann invariants are used. If any component of the magnetic field is close to zero, our code uses a small value for it in the calculation for the set of time-averaged fluxes to avoid the singularity. Since the value is small but within the accuracy of digits of a machine, the resulting magnetic pressure is very small compared to the local thermal pressure.

3.4. A Scheme for Multidimensional Situations

Our two-dimensional scheme is built upon the dimensional splitting method originally suggested by Strang [25]. Each time step of a two-dimensional problem is broken down into one-dimensonal passes in which derivatives in the other direction are set to zero. Each row in the grid is treated as if it was an independent one-dimensional problem. After all the rows in

one direction are applied by the one-dimensional functioning code, another pass in the other direction is made. These x- and y-passes compose the first half time step. In the remaining half time step, the scheme carries out the y-pass first and then the x-pass. For stability of the scheme, the length of the time step may be adjusted only after a complete one time step, i.e., two x-passes and two y-passes.

Each pass (e.g., x-pass) of a two-dimensional scheme updates a set of physical variables including ρ, p, $u_{x,y,z}$, and $B_{y,z}$ by solving Eq. (3a) through the procedures described in our one-dimensional functioning code (Section 3.2). The longitudinal component B_x will be updated in the y-pass of the dimensional splitting method. Unlike the method presented in [14], we have not introduced any source term arising from a varying $\mathbf{B}$ in the direction of spatial integration in each of the one-dimensional passes of the dimensional splitting method. In the nonlinear and linear Riemann solvers described in Section 3.1, the longitudinal component of the magnetic field is assumed to be a constant. In a one-dimensional pass of a two-dimensional simulation, the longitudinal component varies with the space coordinate. The value at an interface after a linear or parabolic interpolation of the longitudinal component may be used for the Riemann problem arising from the interface. Therefore our one-dimensional functioning code is used in each one-dimensional pass of our multidimensional scheme.

3.5. The Divergence-free Condition for the Magnetic Field

The divergence-free condition for the magnetic field is a constraint on an initial condition, not an evolution equation. Although the condition is maintained analytically by the field evolution, it is true only up to a certain accuracy for difference equations. A nonzero divergence is a symptom of numerical error for a difference scheme.

The magnetic field may be solved by evolving either the field itself, or a vector potential. While these two approaches are analytically identical, introducing a vector potential has numerical disadvantages: a staggered grid is necessary, basic equations are not in the form suitable for the characteristic formulations, and the direct derivatives are needed. Because of the direct derivatives, a truncation error of order unity will happen for the magnetic field in the vicinity of a discontinuity. Thus the numerical error for the divergence is still order unity in the vicinity of a discontinuity, although normally no one will suspect the divergence-free condition if a vector potential is introduced.

The key issue for the divergence-free condition is whether or not the divergence will be accumulated in a numerical scheme, not whether or not it is vanishing exactly. Each pass in our scheme conserves the magnetic flux exactly, and the longitudinal component of the magnetic field remains unchanged in a one-dimensional pass. We believe that our multidimensional scheme conserves the magnetic flux. If calculated, the divergence of the magnetic field may be of order unity near a discontinuity because of the truncation of the scheme. The divergence outside a discontinuity may be reduced as small as wanted when the mesh size is reduced. The structure inside a discontinuity is unphysical under ideal equations, and we believe that the structure inside a discontinuity will not influence the rest of a flow for a system without any source or sink, such as ideal MHD equations, as long as the jump conditions for the inflow and outflow are satisfied.

The divergence-free condition in a high-order Godunov scheme has been directly discussed by Zachary *et al.* [14]. Following the prescription in [28], they explicitly introduced a step to ensure the divergence-free condition in their multidimensional scheme based on the dimensional splitting method. After each time step, they solve the Poisson equation for the potential ϕ:

$$\nabla^2\phi + \nabla \cdot \mathbf{B} = 0.$$

Then the new magnetic field is defined by $\mathbf{B} = \mathbf{B} - \nabla\phi$. But, they did not find any noticeable difference whether or not they applied this explicit step for their numerical examples.

We have not introduced any additional step to formally ensure the divergence-free condition in our scheme and we consider such an additional step unnecessary, as indicated by the numerical examples in [14] and discussed above. We will not give any numerical measurement for the divergence in this paper, because the value of the divergence may be calculated only approximately outside a discontinuity, and it is meaningless inside a discontinuity in our formulations. Instead, in Section 4.2.1 we will give one numerical example for the steepening of a wave in a two-dimensional domain to show the conservation of the magnetic flux by the comparison with a one-dimensional result. We will not discuss the divergence further in this paper, although it is a very interesting issue.

4. NUMERICAL EXAMPLES

In this section we will give some numerical examples to show the correctness and performance of the numerical scheme described above, which include both one- and two-dimensional situations. The one-dimensional simulations include the propagation of waves and various shock-tube problems, and two-dimensional problems include the propagation of a one-dimensional wave in a two-dimensional domain, and the interaction between MHD shocks and a cloud.

The ratio of the specific heat capacities γ is set to $\frac{5}{3}$ in all the numerical examples unless it is specified otherwise. Only one iteration in our nonlinear Riemann solver is used in all the examples, although our linear Riemann solver will give equally good results for some of them. The grids used in all the examples are uniform in all the examples. Mach number for a fast (or slow or magnetosonic) shock is defined as the ratio between the shock speed ($s - u_{l0}$) in the reference of the preshock state

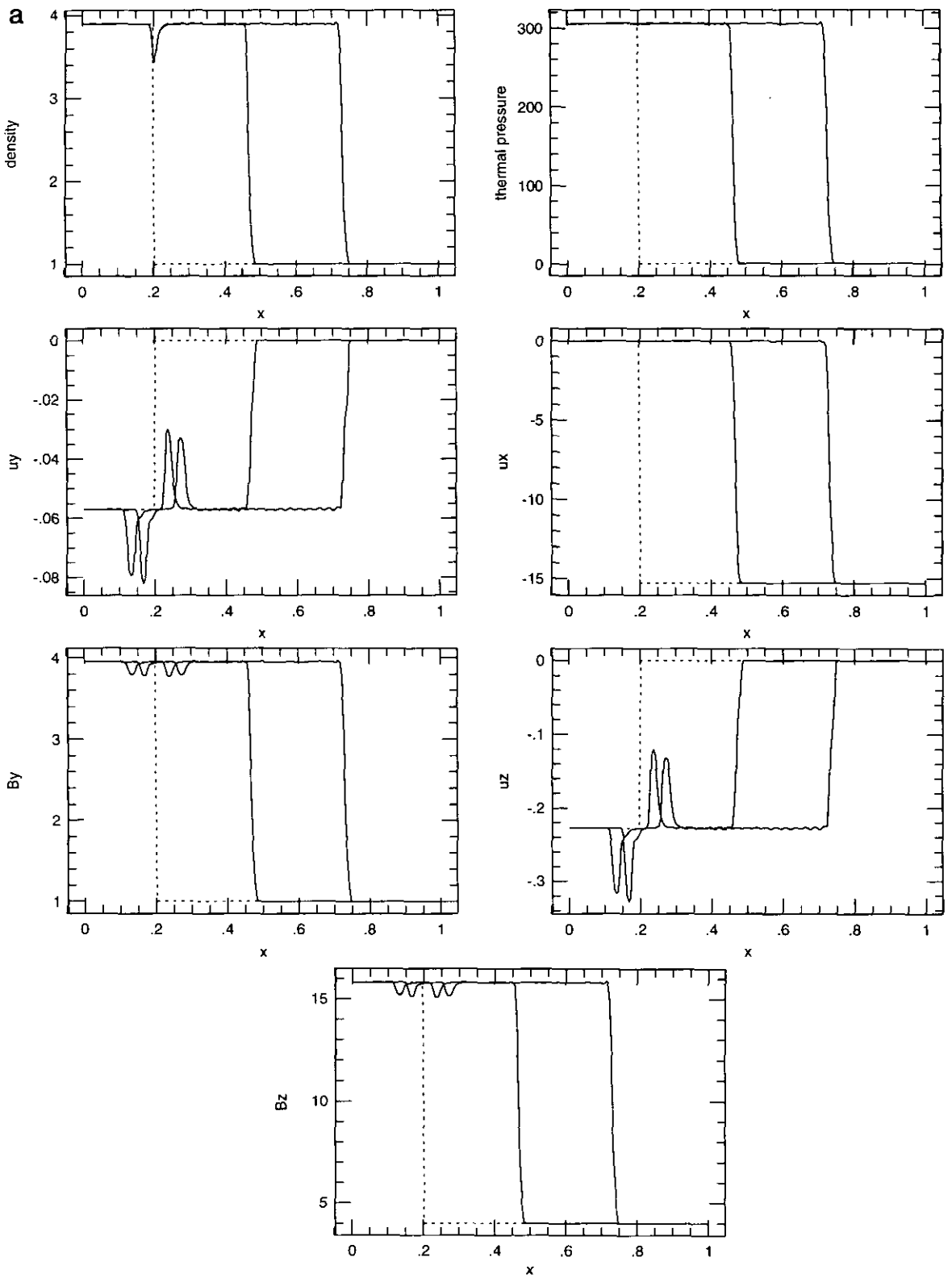

FIG. 4. The propagation of a MHD fast shock: $\gamma = \frac{5}{3}$, $B_x = 5$, Mach number = 10. The dashed lines are the initial conditions and the solid lines are the profiles at $t = 0.05$ and 0.1, respectively. The initial shock (a) is a pure discontinuity; (b) has a small internal structure.

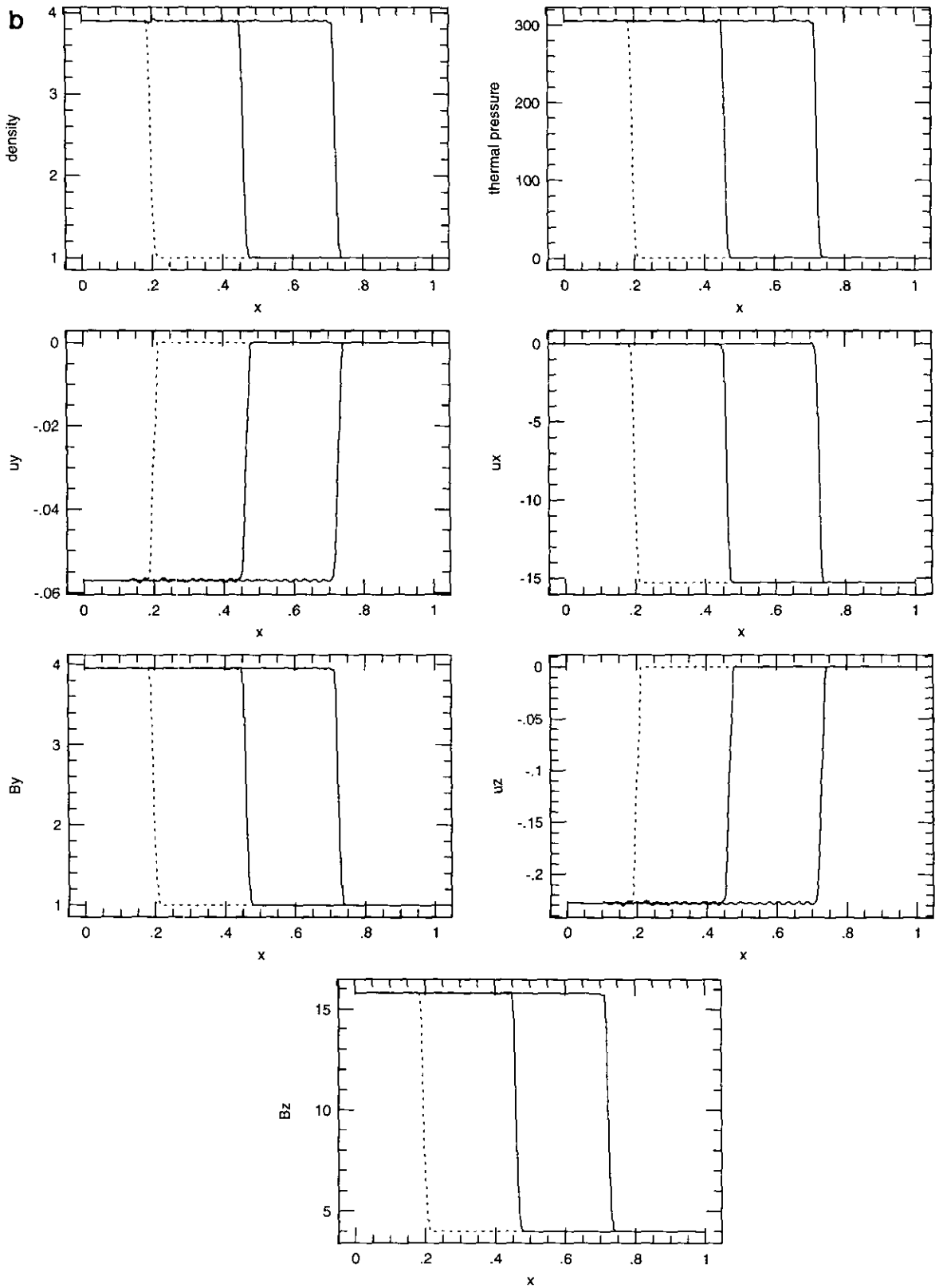

FIG. 4—*Continued*

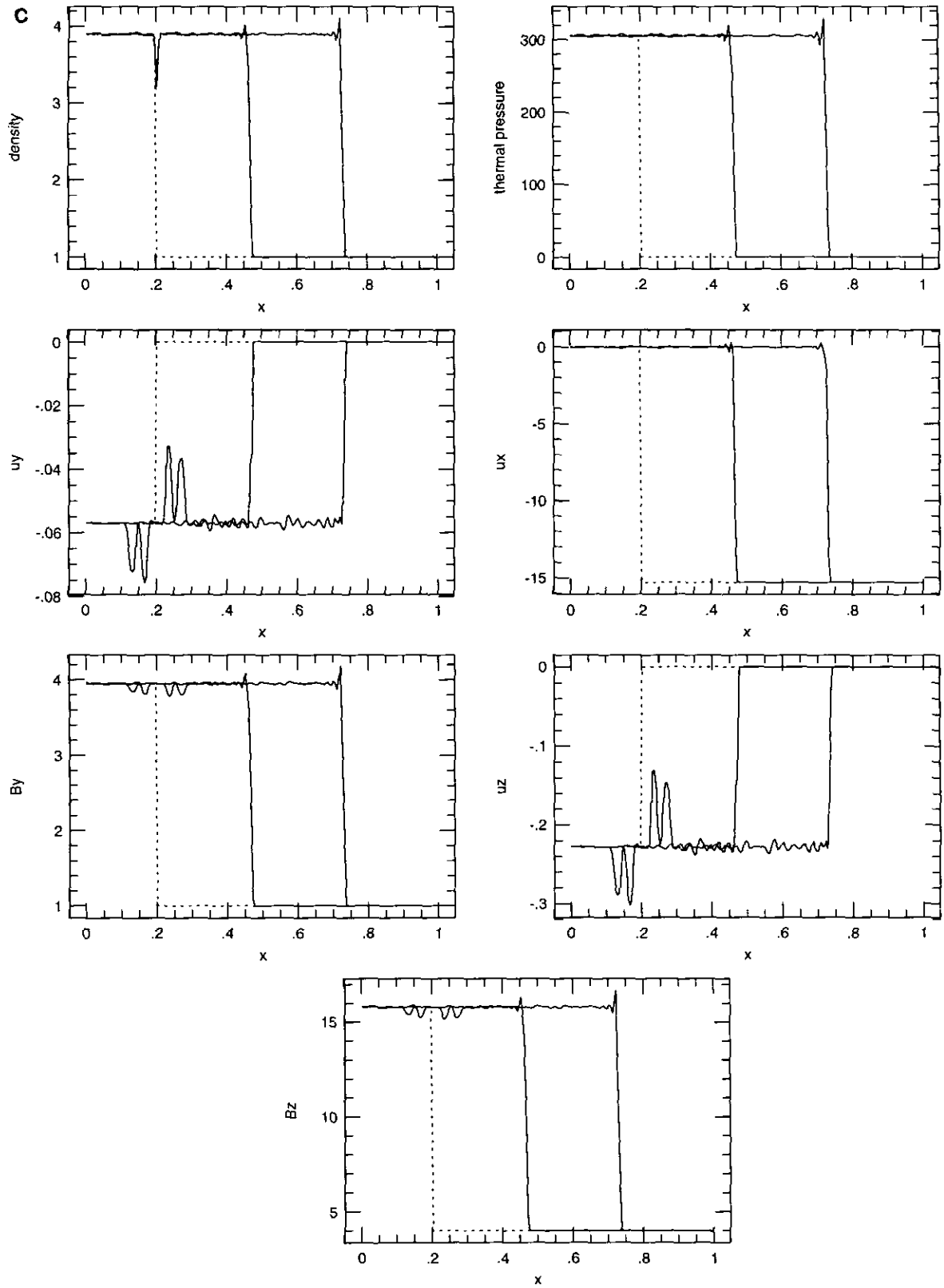

FIG. 4—*Continued*

and the corresponding characteristic speed C_f (or C_s or C_f) in the preshock state, where s is the shock speed and u_{t0} is the longitudinal component of the flow velocity at the preshock state. Since the preshock state may be different from either the left or the right state for a slow shock in a shock-tube problem, it is not always appropriate to consider a Mach number as the ratio between a shock speed and the characteristic speed at the right or left state, or as the ratio between a shock speed and an Alfven wave speed.

4.1. One-Dimensional Situations

The examples to be given in this subsection are to test the correctness and performance of our one-dimensional functioning code for various problems involving strong MHD discontinuities. The periodic boundary conditions are used for the first example and the continuation boundary conditions are used in the others. Two hundred uniform computational zones between zero and unity are used in all the examples unless specified otherwise.

For any numerical scheme designed for shock dynamics, it is important to test the propagation of waves and shocks. Such problems may be difficult because the waves will steepen themselves and because the structure of shocks should be well maintained. We give an example in which the flow starts as perfectly smooth profiles to see how our scheme works for the steepening of a MHD wave. B_x is set to 2 and the Courant number for the stability is set to 0.8 in this example. Initially a slow wave is set up through a set of Riemann invariants

$$\frac{dR_{s+}}{dx} = -0.2(2\pi)\cos(2\pi x),$$

$$\frac{d}{dx} R_{0,f\pm,s-,a\pm} \equiv 0.$$

The initial conditions for normal physical variables are obtained by solving the set of ordinary differential equations defined by these Riemann invariants and the values (1, 1, −0.3938, 0, 0, 4, 2) for $(\rho, p, u_x, u_y, u_z, B_y, B_z)$ at $x = 0$. The initial conditions thus obtained are plotted by the dashed lines in Fig. 3. Since the wave has a finite amplitude, the initial profiles in the figure are not exactly sinusoidal although R_{s+} is. Five profiles with time interval 1.27 during which the wave propagates about a half wavelength show the steepening of the wave.

In order to see difference between two kinds of interpolation described in Section 2.2, one for Riemann invariants and the

−15.30, 0, 0, 1, 4) for $x > 0.2$ with B_x being 5, which represents a fast shock with a Mach number 10. One iteration in the Riemann solver is used and the Courant number is set to 0.5 in this example. Figure 4a shows the initial profiles by dashed lines and the profiles at $t = 0.05$ and 0.1 by solid lines, respectively. It may be seen that the shock travels rightward generating very little numerical noise. Both the compression and the shearing of the fluid are responsible for the increase of the transverse components of magnetic field from the preshock state to the postshock state. Note that there are MHD waves generated near $x = 0.2$, which are related to the Riemann invariants with the slow wave speed and the zero wave speed. The amplitudes of the slow waves in the transverse flow velocities are small compared to the jump in u_x for the fast shock.

The waves near $x = 0.2$ in Fig. 4a should be viewed as "starting errors" arising from the purely discontinuous initial conditions for this problem. The initial conditions for this example contain only one fast shock. Initially the shock is assumed to have no internal structure and the shock front coincides with the interface of two neighboring zones. The Riemann solver can successfully solve the initial Riemann problem and get the correct solution which contains only one fast shock. After the first time step, however, the single discontinuity spreads over one computational zone, since our algorithm keeps track of only the average values over each zone. Thus three states are obtained just after the first time step. The states in the left and the right regions are the same as the left and right states of the initial conditions, while the state in the middle region is different from either the left or the right state. Either Riemann problem consisting of the left two or right two states involves one fast shock as well as weak slow waves. Fortunately, the overall result is equivalent to the original fast shock, and if we give the initial shock a small internal structure as is generated by the numerical scheme, all the waves are dramatically reduced except the original fast shock. Figure 4b shows the results of the simulation when we give the initial shock in Fig. 4a a small internal structure.

In order to show the effect of the artificial viscosity, we also simulated the propagation of the shock without the artificial viscosity. The results (not given) show the fluctuations in the immediate postshock state, and the amplitude of the fluctuation is within 5% of the jumps.

To investigate the properties of the numerical scheme for the propagation of a MHD slow shock, we give the following initial conditions which represent a slow shock with a Mach number of 3.5 at $x = 0.2$: $(\rho, p, u_x, u_y, u_z, B_y, B_z)$ is (3.108,

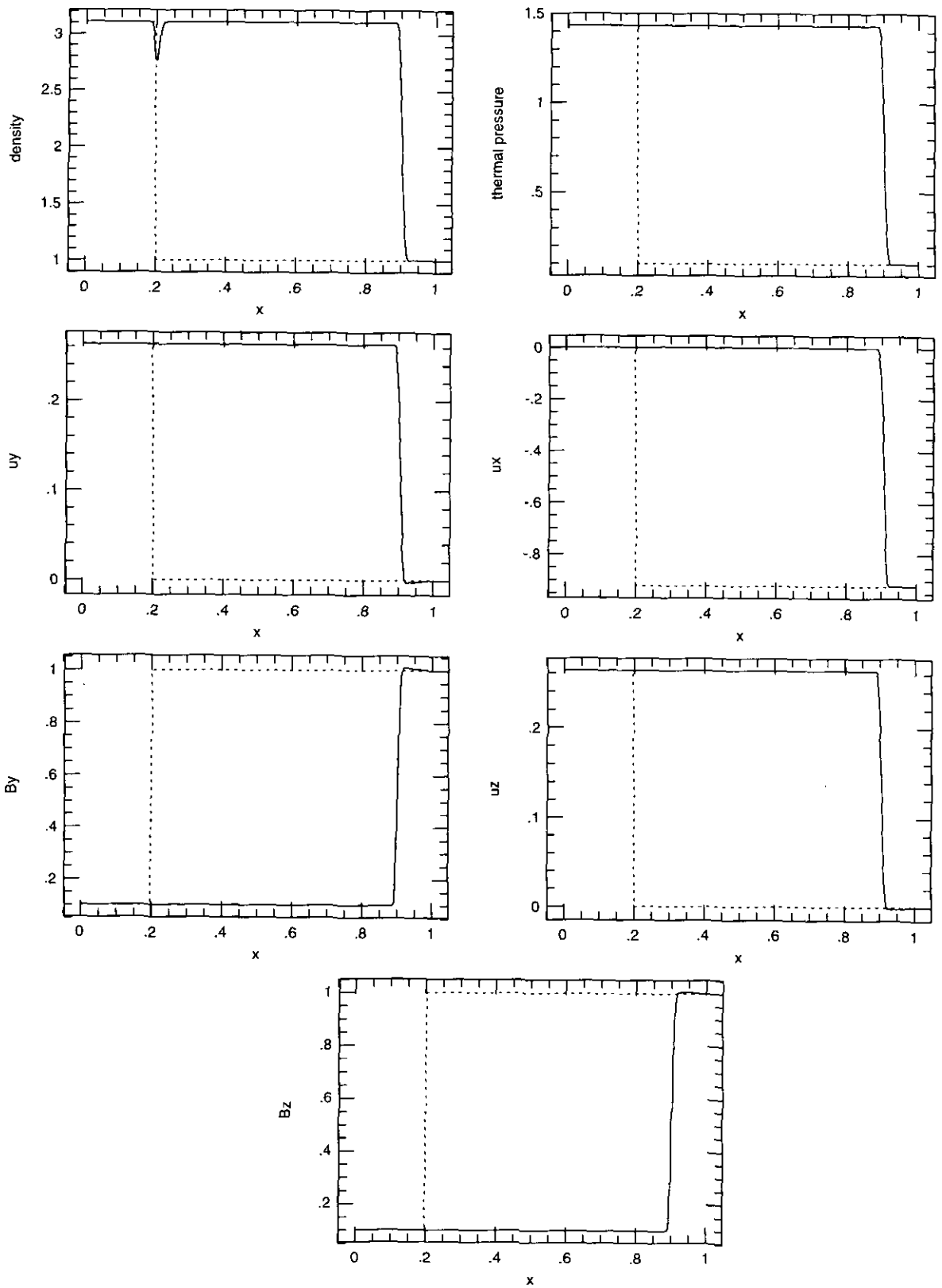

FIG. 5. The propagation of a MHD slow shock: $\gamma = \frac{5}{3}$, $B_x = 5$, Mach number = 3.47. The solid lines are the profiles at $t = 1.6$.

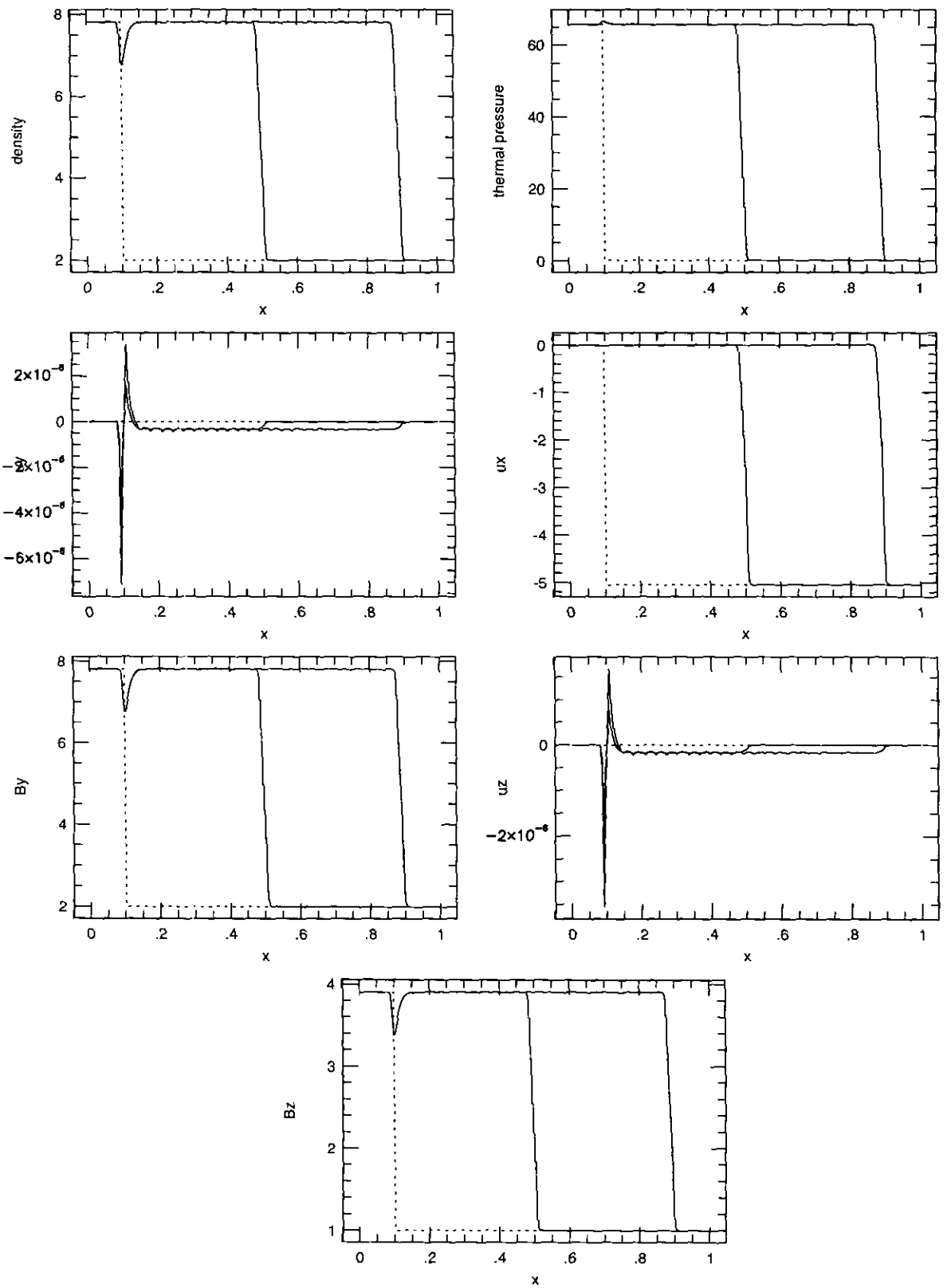

FIG. 6. The propagation of a magnetosonic shock: $\gamma = \frac{5}{3}$, $B_x = 0$, Mach number = 12.76. The solid lines are the profiles at $t = 0.225$ and 0.45, respectively.

TABLE I

The Exact Solutions for the Riemann Problem in Fig. 7[a]

Regions	ρ	p	ux	uy	uz	By	Bz
L	1.500E − 01	2.800E − 01	2.155E + 01	1.000E + 00	1.000E + 00	−2.000E + 00	−1.000E + 00
R2	5.853E − 01	9.112E + 01	3.773E − 05	1.000E + 00	1.000E + 00	−7.803E + 00	−3.902E + 00
R3	3.929E − 01	9.107E + 01	3.773E − 05	0.000E + 00	0.000E + 00	7.858E + 00	3.929E + 00
R	1.000E − 01	1.000E − 01	−2.645E + 01	0.000E + 00	0.000E + 00	2.000E + 00	1.000E + 00

[a] $B_x = 0$, $\gamma = \frac{5}{3}$.

TABLE II

The Exact Solutions for the Riemann Problem in Fig. 8[a]

Regions	ρ	p	ux	uy	uz	By	Bz
L	3.200E − 01	1.483E + 01	−4.678E − 05	1.910E + 00	9.551E − 01	2.239E + 00	1.120E + 00
R2	3.200E − 01	1.483E + 01	−4.678E − 05	1.910E + 00	9.551E − 01	2.239E + 00	1.120E + 00
R3	3.580E − 01	1.228E + 01	−9.688E − 02	−6.078E − 01	−3.039E − 01	7.463E + 00	3.732E + 00
R	1.000E − 01	1.000E − 01	−1.041E + 01	0.000E + 00	0.000E + 00	2.000E + 00	1.000E + 00

[a] $B_x = 2$, $\gamma = \frac{5}{3}$.

shock has no internal structure, the plot for the density displays one unwanted structure, which arises from the purely discontinuous initial conditions and may be reduced by introducing a small internal structure in the initial shock.

Figure 6 shows the results for the propagation of a magnetosonic shock with a Mach number of 12.8, which is represented initially by the following left and right states: $(\rho, p, u_x, u_y, u_z, B_y, B_z) = (7.8073, 65.7254, 0, 0, 0, 7.8073, 3.9036)$ for $x < 0.1$ and $(2, 0.1, -5.0459, 0, 0, 2, 1)$ $x > 0.1$ with vanishing B_x. The dashed lines in the figure are the initial conditions and the solid lines are the profiles at $t = 0.225$ and 0.45, respectively. The waves near $x = 0.1$ may be reduced by introducing a small internal structure in the initial shock.

Another standard test for numerical schemes designed for

TABLE III

The Exact Solutions for the Riemann Problem in Fig. 9[a]

Regions	ρ	p	ux	uy	uz	By	Bz
L	2.000E − 01	1.079E + 01	4.589E + 00	−2.061E + 00	3.317E + 00	3.800E + 00	3.800E + 00
R2	2.000E − 01	1.079E + 01	4.589E + 00	−1.081E + 00	1.215E + 00	5.354E + 00	4.684E − 01
R3	3.601E − 01	1.079E + 01	4.589E + 00	−1.081E + 00	1.215E + 00	5.354E + 00	4.684E − 01
R4	3.601E − 01	1.079E + 01	4.589E + 00	−3.507E − 01	−3.507E − 01	3.800E + 00	3.800E + 00
R	1.000E − 01	2.000E − 01	−4.589E + 00	0.000E + 00	0.000E + 00	1.000E + 00	1.000E + 00

[a] $B_x = 2$, $\gamma = \frac{5}{3}$.

TABLE IV

The Exact Solutions for the Riemann Problem in Fig. 10[a]

Regions	ρ	p	ux	uy	uz	By	Bz
L	1.000E + 00	1.000E + 00	3.687E + 01	−1.546E − 01	−3.864E − 02	4.000E + 00	1.000E + 00
R2	3.982E + 00	1.806E + 03	0.000E + 00	−7.727E − 02	−1.932E − 02	1.595E + 01	3.988E + 00
R	1.000E + 00	1.000E + 00	3.687E + 01	0.000E + 00	0.000E + 00	4.000E + 00	1.000E + 00

[a] $B_x = 4$, $\gamma = \frac{5}{3}$.

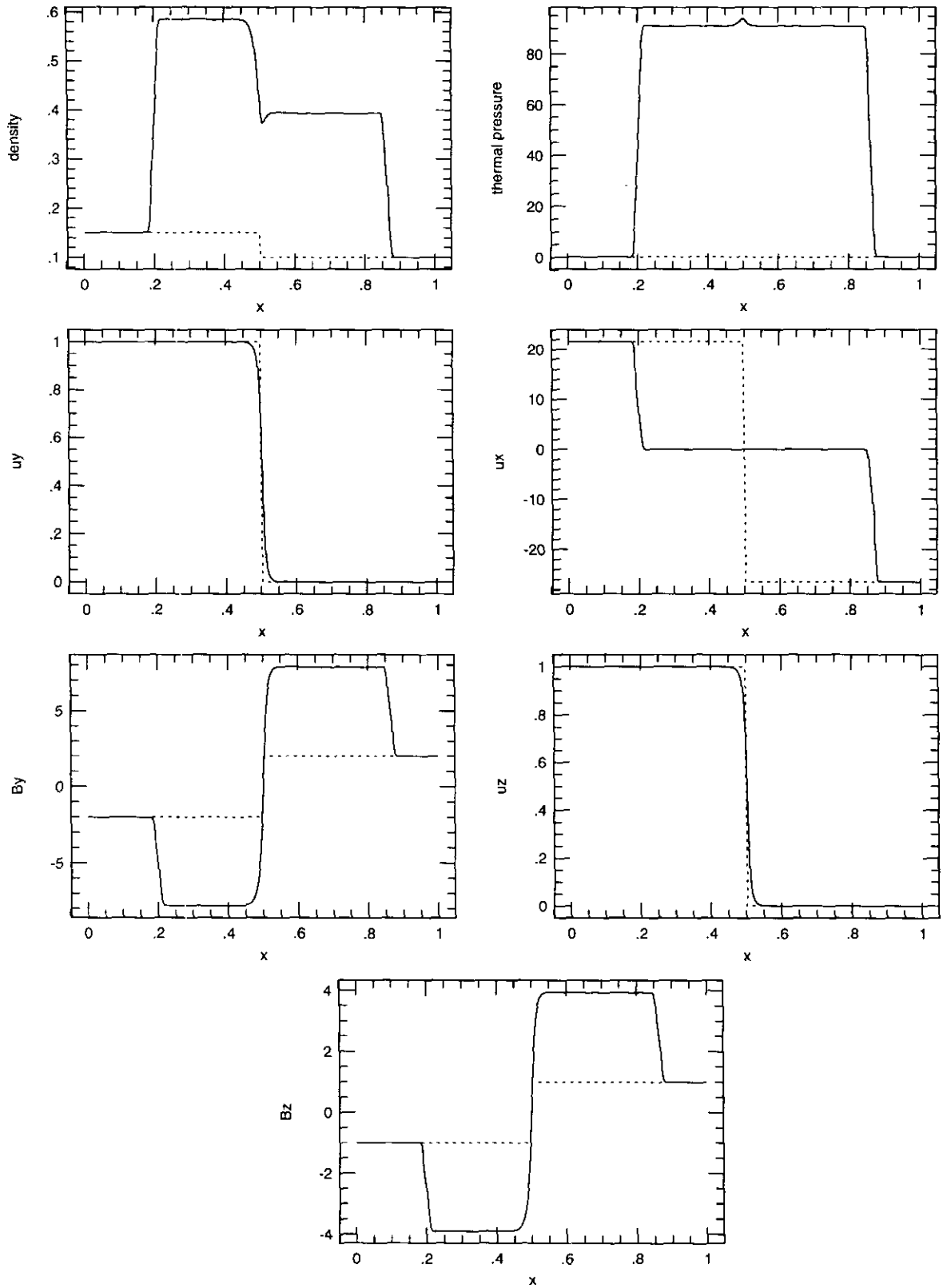

FIG. 7. The generation of two magnetosonic shocks with Mach numbers 12 and 14.9 and one tangential discontinuity: $\gamma = \frac{5}{3}$, $B_x = 0$. Initial conditions: $(\rho\ p,\ u_x,\ u_y,\ u_z,\ B_y,\ B_z) = (1.5,\ 0.28,\ 21.55,\ 1,\ 1,\ -2,\ -1)$ for $x < 0.5$ and $(0.1,\ 0.1,\ -26.45,\ 0,\ 0,\ 0,\ 2,\ 1)$ for $x > 0.5$. The solid lines are the profiles at $t = 0.04$. The exact solutions for the states in regions R2 and R3 are shown in Table I.

shock dynamics is a shock-tube problem, i.e., the generation of multiple discontinuities or rarefaction waves from an initial discontinuity. Figures 7–12 show the results from our simulations for various shock-tube problems. Their initial left and right states in the shock tube problems are shown in Tables I–VI, respectively, where L and R stand for the left and right states. The dashed lines in these figures are initial conditions, and the solid lines are the plots at some later time. The Courant number for stability is set to 0.6 in all these shock-tube problems.

Figure 7 shows one magnetosonic shock traveling leftward with a Mach number of 12, another magnetosonic shock propagating to the right with a Mach number of 14.9, and one tangential discontinuity at $t = 0.04$. Figure 8 displays results at $t = 0.16$ which contain one fast shock with a Mach number of 5, one slow shock with a Mach number of 1.1, and one contact discontinuity. The generation of two rotational discontinuities, one fast shock and one contact discontinuity is shown in Fig. 9 which contains the plots at $t = 0.08$. Across either rotational discontinuity, the transverse part of the magnetic field rotates 40°. The fast shock has a Mach number of 5.0. Two fast shocks with a Mach number of 25.5 each may be found in Fig. 10. We should mention that the structure near $x = 0$ in Fig. 10 is the starting error due to the pure discontinuity in the initial condition. Figure 11 shows the generation of two fast shocks with Mach numbers of 3.15 and 3.19, two slow shocks with Mach numbers 1.15 and 1.3, and one contact discontinuity at $t = 0.4$. The maximum number of discontinuities which may be generated from any MHD shock-tube problem is seven. Figure 12 shows seven discontinuities in one shock-tube problem at $t = 0.15$, where two fast shocks have Mach numbers of 1.84 and 2.01, two slow shocks have Mach numbers of 1.38 and 1.49, and across either rotational discontinuity the transverse part of the magnetic field undergoes a 35° rotation. Four hundred computational zones between zero and unity have been used in this example in order to separate the fine structure between the slow shocks and the rotational discontinuities.

All the discontinuities in each of Figs. 7–12 divide the whole x-space into several different regions. The physical states are nearly constant at these different regions. For example, the three discontinuities in Fig. 7 divide the x-space into four different regions: L, R2, R3, and R. Tables I–VI give the solutions in these regions for the Riemann problem with these left and right states. It is easy to see that the states in the different regions in each of Figs. 7–12 have good agreement with the solutions in its corresponding table.

For the purpose of comparison with the solutions of the corresponding Riemann problems, all the shock-tube problems we have given do not involve rarefaction waves since the solutions of the Riemann problems may be found using our nonlinear Riemann solver. Although we approximate rarefaction waves as rarefaction shocks when we calculate the time-averaged fluxes in the MHD Riemann solver, the scheme does work for rarefaction waves. In Fig. 13 we give the results at $t = 0.1$ of the problem studied by previous investigators [11, 13, 14] which is a MHD analogue of the Sod shock tube-problem [26]. The initial conditions are $(\rho, p, u_x, u_y, u_z, B_y, B_z) = (1, 1, 0, 0, 0, \sqrt{4\pi}, 0)$ for $x < 0.5$ and $(1, 0.1, 0, 0, 0, -\sqrt{4\pi}, 0)$ for $x > 0.5$ with $B_x = 0.75\sqrt{4\pi}$. The ratio of specific heats is chosen to be $\gamma = 2$ for comparison with the previous investigation. Eight hundred zones have been used in this example, as used by the previous investigators. The Courant number is set to 0.8 and no artificial viscosity is used in this example.

Our scheme does not contain any formulation for compound waves. It is interesting to note that if we consider the two postwave states for the two fast rarefaction waves in the solution as the left and right states for a Riemann problem, the solutions of the Riemann problem obtained by our Riemann solver through enough iterations will be exact; it contains a rotational discontinuity with 180° as well as the slow waves. But the result of our 1D simulation shows the compound wave. As we know, a discontinuity represented by the zone-averages in a numerical calculation are not purely rotational discontinuity after the first time step if there is an initial discontinuity. Thus numerical procedures introduce some kind of disturbance to the rotational discontinuity. The nature of the instability of a rotational discontinuity with a large rotated angle and the numerical viscosity/resistivity intrinsically existing in a Godunov scheme is responsible for the compound wave.

4.2. Two-Dimensional Situations

In order to test our two-dimensional scheme which is built upon the one-dimensional functioning code, we give two numerical examples: the propagation of a one-dimensional wave in a 2D domain, and the interaction between MHD shocks and a cloud. The first example is of importance for the correctness of the scheme since its correct solution may be obtained by a one-dimensional simulation described in Section 3.2, and the second is to test the performance of our scheme for a problem involving the interaction between strong shocks.

4.2.1. *The Propagation of a Wave*

The propagation of a one-dimensional fast wave is simulated in a two-dimensional domain initially by a fast wave with unity wavelength obliquely propagating in the domain at an angle $\alpha = 30°$ with respect to the x-axis (Fig. 14). The longitudinal component of the magnetic field, B_ξ, is set to 4. The initial wave is obtained through the set of Riemann invariants,

$$\frac{dR_{f+}}{d\xi} = -3.5(2\pi)\cos(2\pi\xi),$$

$$\frac{d}{d\xi}R_{0,s\pm,f-,a\pm} \equiv 0$$

with the values (1, 1, 0, 0, 0, 4, 2) for $(\rho, p, u_\xi, u_\eta, u_z, B_\eta, B_z)$ at the point $(x, y) = (0, 0)$, where u_ξ is the longitudinal

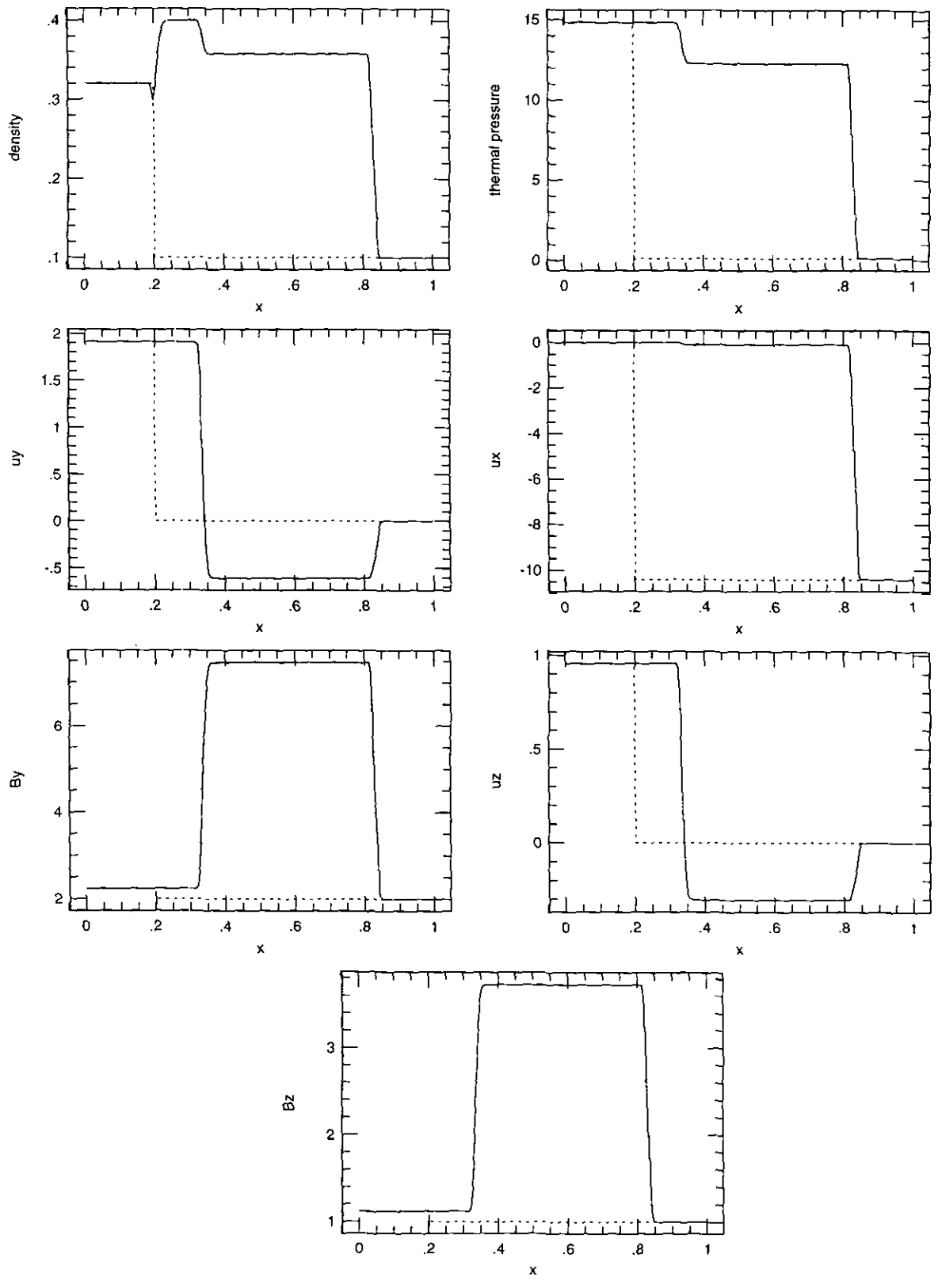

FIG. 8. The generation of one fast shock with a Mach number 5, one slow shock with a Mach number 1.1, and one contact discontinuity: $\gamma = \frac{5}{3}$, $B_x = 2$. Initial conditions: $(\rho\ p,\ u_x,\ u_y,\ u_z,\ B_y,\ B_z) = (0.32,\ 14.83,\ 0,\ 1.91,\ 0.9551,\ 2.239,\ 1.12)$ for $x < 0.20$ and $(0.1,\ 0.1,\ -10.41,\ 0,\ 2,\ 1)$ for $x > 0.20$. The solid lines are the profiles at $t = 0.16$. The exact solutions for the states in regions R2 and R3 are shown in Table II.

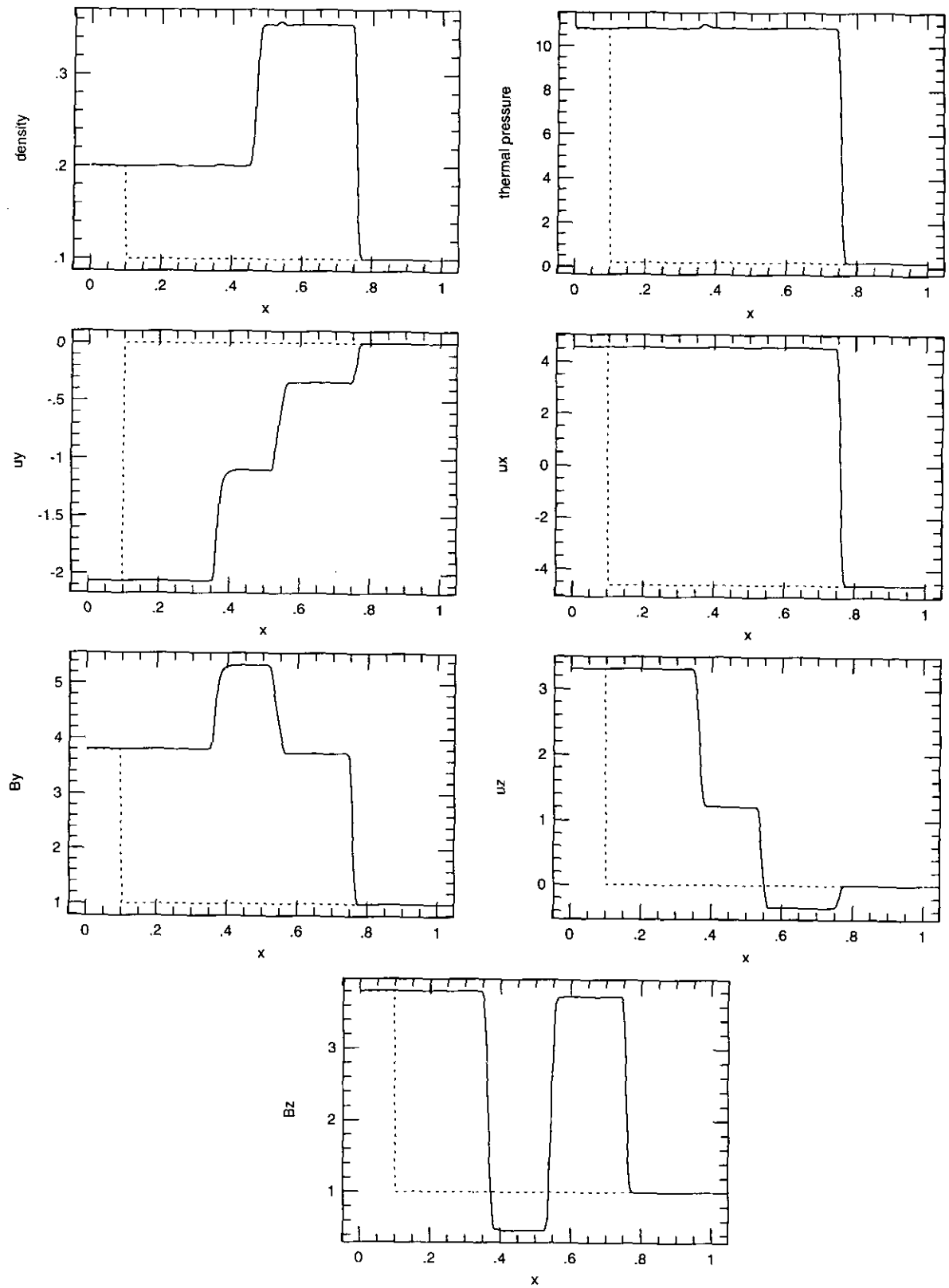

FIG. 9. The generation of one fast shock with a Mach number 5, two rotational discontinuities, and one contact discontinuity: $\gamma = \frac{5}{3}$, $B_x = 2$. Initial conditions: $(\rho\ p,\ u_x,\ u_y,\ u_z,\ B_y,\ B_z) = (2,\ 10.79,\ 4.589,\ -2.061,\ 3.317,\ 3.8,\ 3.8)$ for $x < 0.1$ and $(0.1,\ 0.2,\ -4.589,\ 0,\ 0,\ 1,\ 1)$ for $x > 0.1$. The solid lines are the profiles at $t = 0.08$. Across either rotational discontinuity the transverse part of the magnetic field undergoes 40° rotation. The exact solutions for the states in R2, R3, R4 are shown in Table III.

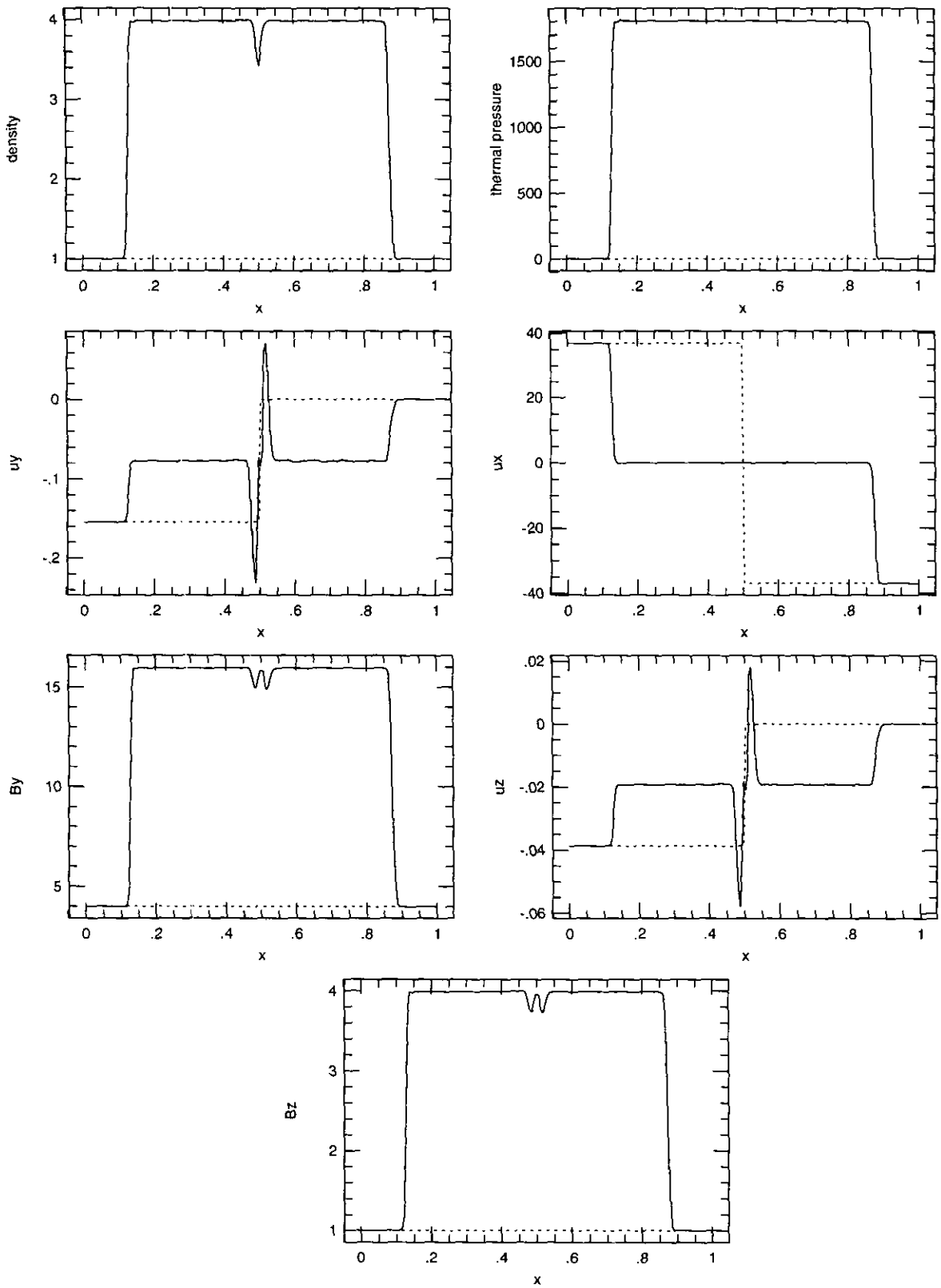

FIG. 10. The generation of two fast shocks of a Mach number 25.5 each: $\gamma = \frac{5}{3}$, $B_x = 4$. Initial conditions: $(\rho\ p,\ u_x,\ u_y,\ u_z,\ B_y,\ B_z) = (1,\ 1,\ 3.687,\ -0.0155,\ -0.00386,\ 4,\ 1)$ for $x < 0.5$ and $(1,\ 1,\ -3.687,\ 0,\ 0,\ 4,\ 1)$ for $x > 0.5$. The solid lines are the profiles at $t = 0.03$. The exact solutions for the state in R2 are shown in Table IV.

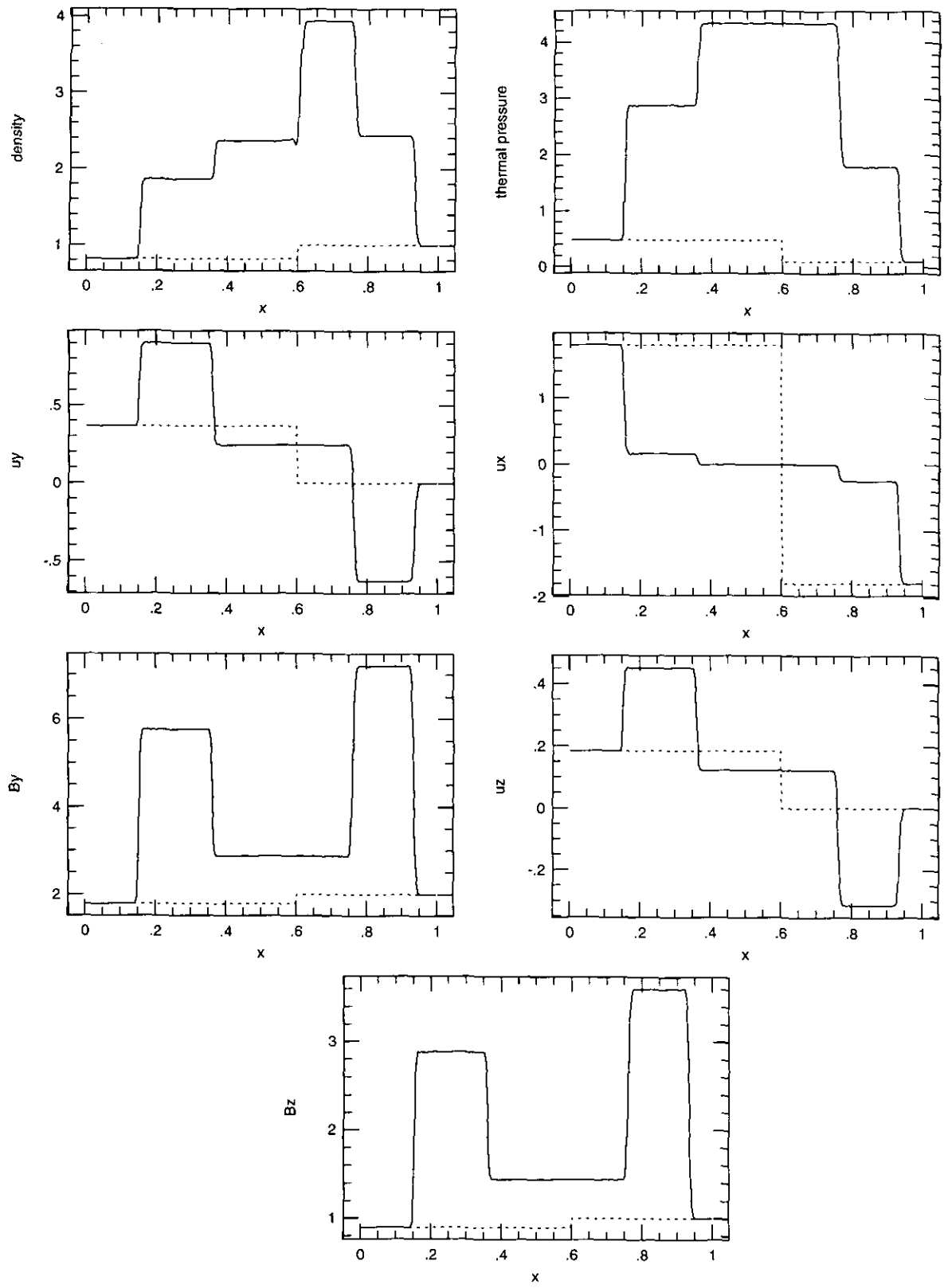

FIG. 11. The generation of two fast shocks with Mach numbers 3.15 and 3.19, two slow shocks with Mach numbers 1.15 and 1.3, and one contact discontinuity. $\gamma = \frac{5}{3}$, $B_x = 4$. Initial conditions: $(\rho\ p,\ u_x,\ u_y,\ u_z,\ B_y,\ B_z) = (0.8129,\ 0.4809,\ 1.801,\ 0.3672,\ 0.1836,\ 1.7856,\ 0.8928)$ for $x < 0.6$ and $(1,\ 0.1,\ -1.7942,\ 0,\ 0,\ 2,\ 1)$ for $x > 0.6$. The solid lines are the profiles at $t = 0.4$. The exact solutions for the states in regions R2, R3, R4, and R5 are shown in Table V.

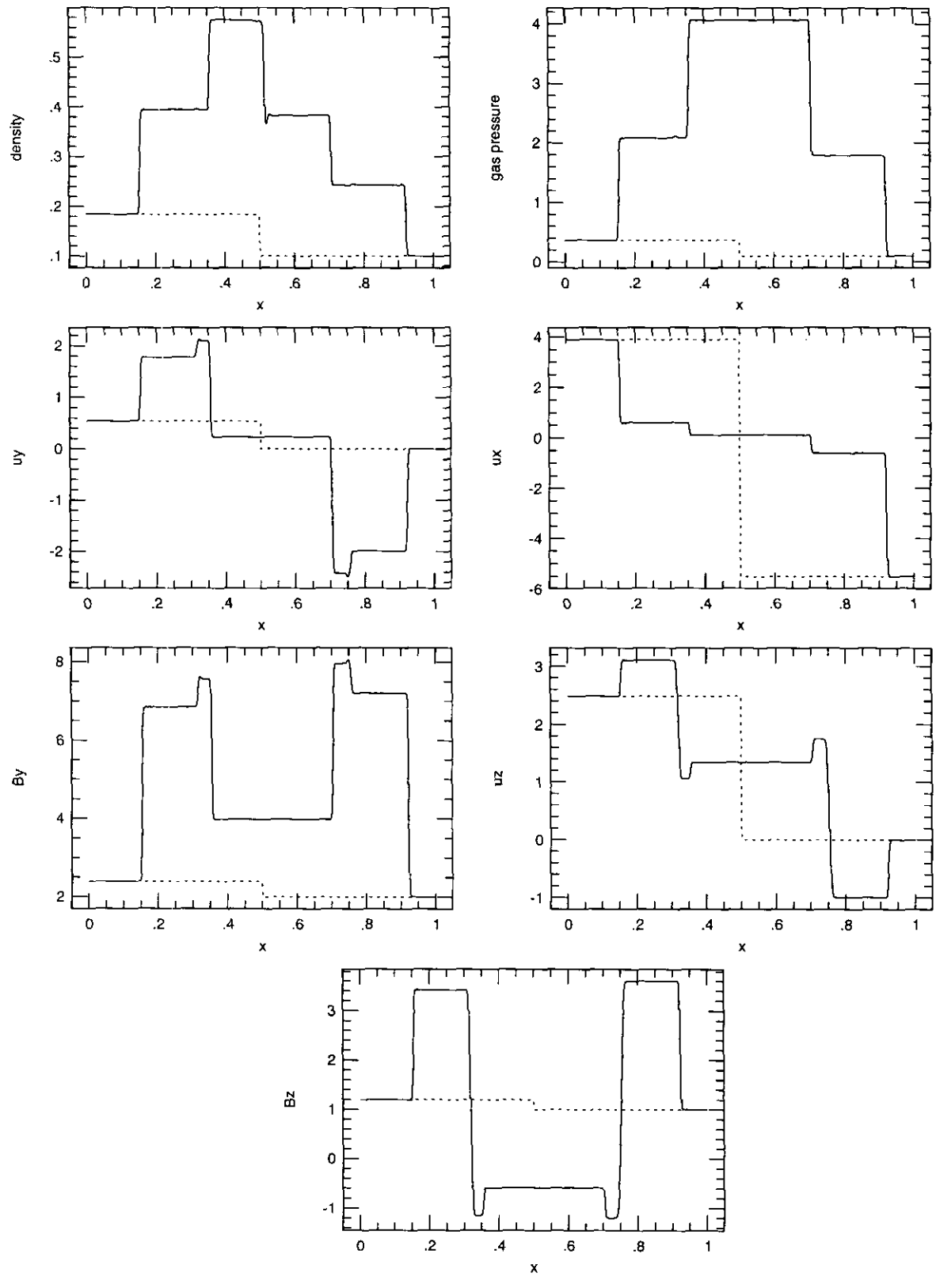

FIG. 12. The generation of seven discontinuities, 400 zones. $\gamma = \frac{5}{3}$, $B_x = 4$. Initially $(\rho\ p,\ u_x,\ u_y,\ u_z,\ B_y,\ B_z) = (0.18405,\ 0.3641,\ 3.8964,\ 0.5361,\ 2.4866,\ 2.394,\ 1.197)$ for $x < 0.5$ and $(0.1,\ 0.1,\ -5.5,\ 0,\ 0,\ 2,\ 1)$ for $x > 0.5$. The solid lines are the profiles at $t = 0.15$. Two fast shocks travel leftward and rightward with Mach numbers 1.84 and 2.01, respectively, and two slow shocks travels leftward and rightward with Mach numbers 1.38 and 1.49, respectively. Across either rotational discontinuity, the transverse part of the magnetic field undergoes 35° rotation. The exact solutions at all the regions (from R2 to R7) are shown in Table VI.

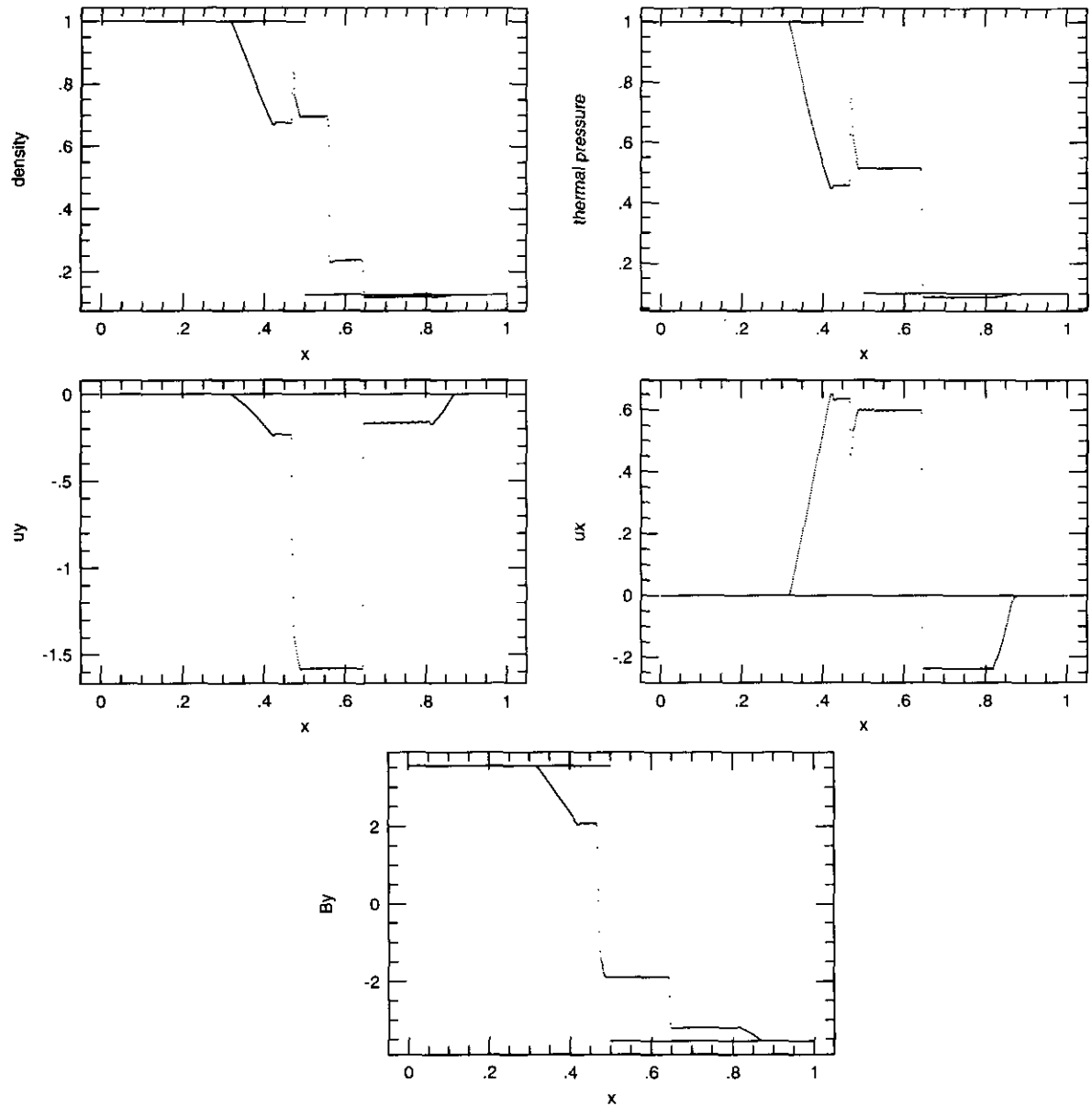

FIG. 13. The problems studied by Brio and Wu: 800 zones, $\gamma = 2$, $B_x = 0.75\sqrt{4\pi}$. Initial conditions: $(\rho\ p,\ u_x,\ u_y,\ u_z,\ B_y,\ B_z) = (1,\ 1,\ 0,\ 0,\ 0,\ \sqrt{4\pi},\ 0)$ for $x < 0.5$ and $(0.1,\ 1,\ 0,\ 0,\ 0,\ -\sqrt{4\pi},\ 0)$ for $x > 0.5$. The solid lines are initial conditions, and the dots are the results at $t = 0.1$.

component of the flow velocity, u_z and B_z are the components perpendicular the simulation domain of the flow velocity and the magnetic field, u_η and B_η are their other transverse components; ξ is the only space coordinate of the one-dimensional wave (see Fig. 14). The x- and y-components of the magnetic field (or the flow velocity) may be obtained by the projection:

$$B_x = B_\xi \cos\alpha - B_\eta \sin\alpha, \tag{11a}$$

$$B_y = B_\xi \sin\alpha + B_\eta \cos\alpha. \tag{11b}$$

The simulation is performed on a $(x_{\max} - 0) \times (y_{\max} -$

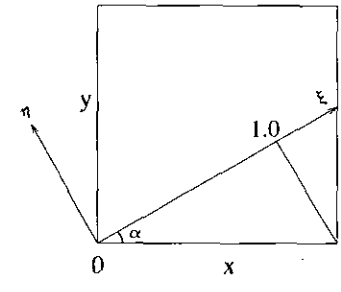

FIG. 14. The geometry in the propagation of a wave in a two-dimensional domain.

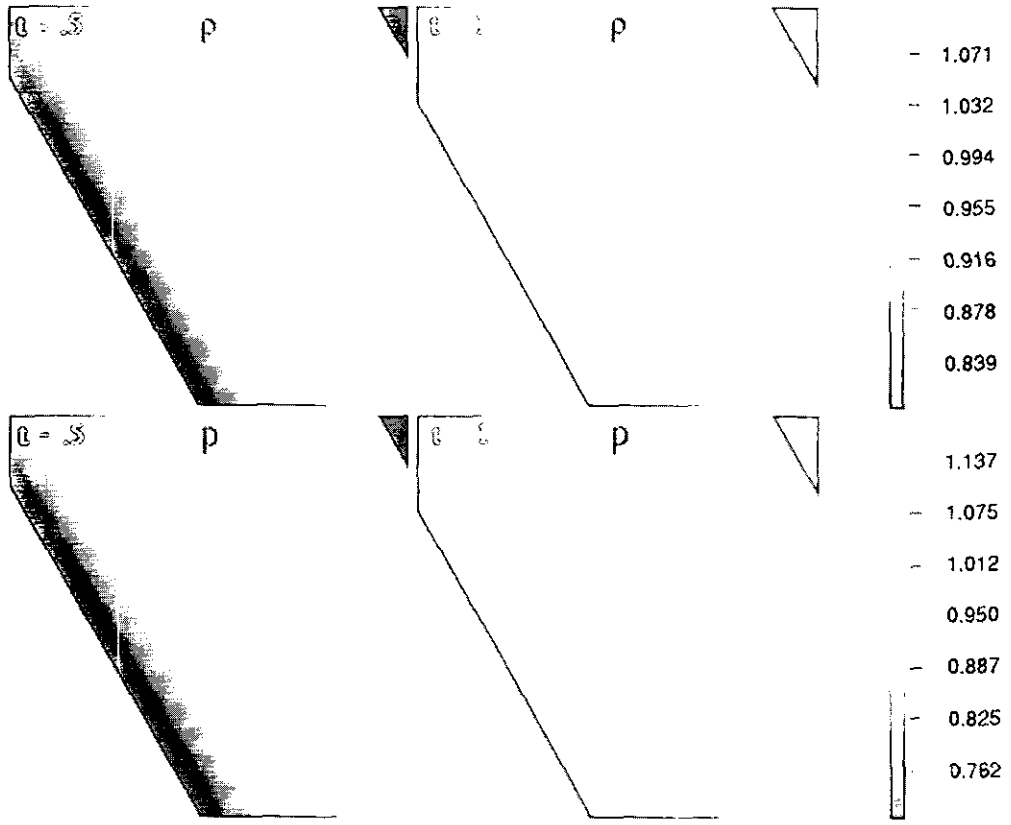

FIG. 15. A wave in a two-dimensional domain. The distributions of the mass density ρ and thermal pressure p at $t = 0.5$ and $t = 1.0$.

0) domain with $x_{max} = y_{max} = 1/\cos\alpha$ and 256×256 uniform computational zones. Periodic boundary conditions are used at the left and right sides of the domain. The boundary conditions at the top and bottom sides are implemented in the following way

wavelength(s), respectively. Figure 17 shows the profiles along the line $y = 128$ zones at the initial time (dashed lines) and at $t = 0.5, 1.0$ (solid lines). The wave becomes a shock after it has traveled about a wavelength. In order to check the correctness of

TABLE VI

The Exact Solutions for the Riemann Problem in Fig. 12[a]

Regions	ρ	p	ux	uy	uz	By	Bz
L	1.841E − 01	3.641E − 01	3.896E + 00	5.361E − 01	2.487E + 00	2.394E + 00	1.197E + 00
R2	3.939E − 01	2.083E + 00	5.971E − 01	1.778E + 00	3.107E + 00	6.840E + 00	3.420E + 00
R3	3.939E − 01	2.083E + 00	5.971E − 01	2.103E + 00	1.066E + 00	7.565E + 00	−1.122E + 00
R4	5.750E − 01	4.062E + 00	1.097E − 01	2.322E − 01	1.344E + 00	3.981E + 00	−5.904E − 01
R5	3.833E − 01	4.062E + 00	1.097E − 01	2.322E − 01	1.344E + 00	3.981E + 00	−5.904E − 01
R6	2.433E − 01	1.788E + 00	−6.053E − 01	−2.428E + 00	1.738E + 00	7.963E + 00	−1.181E + 00
R7	2.433E − 01	1.788E + 00	−6.053E − 01	−1.992E + 00	−9.960E − 01	7.200E + 00	3.600E + 00
R	1.000E − 01	1.000E − 01	−5.500E + 00	0.000E + 00	0.000E + 00	2.000E + 00	1.000E + 00

[a] $B_x \approx 4$, $\gamma = \frac{5}{3}$.

$$\frac{d}{d\xi} R_{0,s\pm,f-,a\pm} \equiv 0$$

with values (1.09904e + 00, 1.17046e + 00, 1.92927e − 01, −8.48155e − 02, −4.24078e − 02, 4.57010e + 00, 2.28528e + 00) for $(\rho, p, u_\xi, u_\eta, B_\eta, B_z)$ at $\xi = 0$ and $B_\xi = 4$. The initial conditions in the one-dimensional simulation correspond to the initial values at the point $(x, y) = (0, y_{max}/2)$ in the two-dimensional simulation. The projection of the results of the one-dimensional simulation at $t = 0.5$ and 1.0 are also plotted in Fig. 17 (dotted lines), which are hard to see because of the solid lines in the figure. B_x and B_y from the one-dimensional simulation are calculated by Eqs. (11a)(11b). For the comparison, the horizontal coordinate for the dotted lines is $\xi/\cos\alpha$. The concurrence between the solid and dotted lines in the figure indicates the correctness of our multidimensional scheme on the problem.

4.2.2. *Interaction between MHD Shocks and a Cloud*

Our numerical scheme is intentionally designed for MHD problems involving strong shocks. In order to test the perfor-

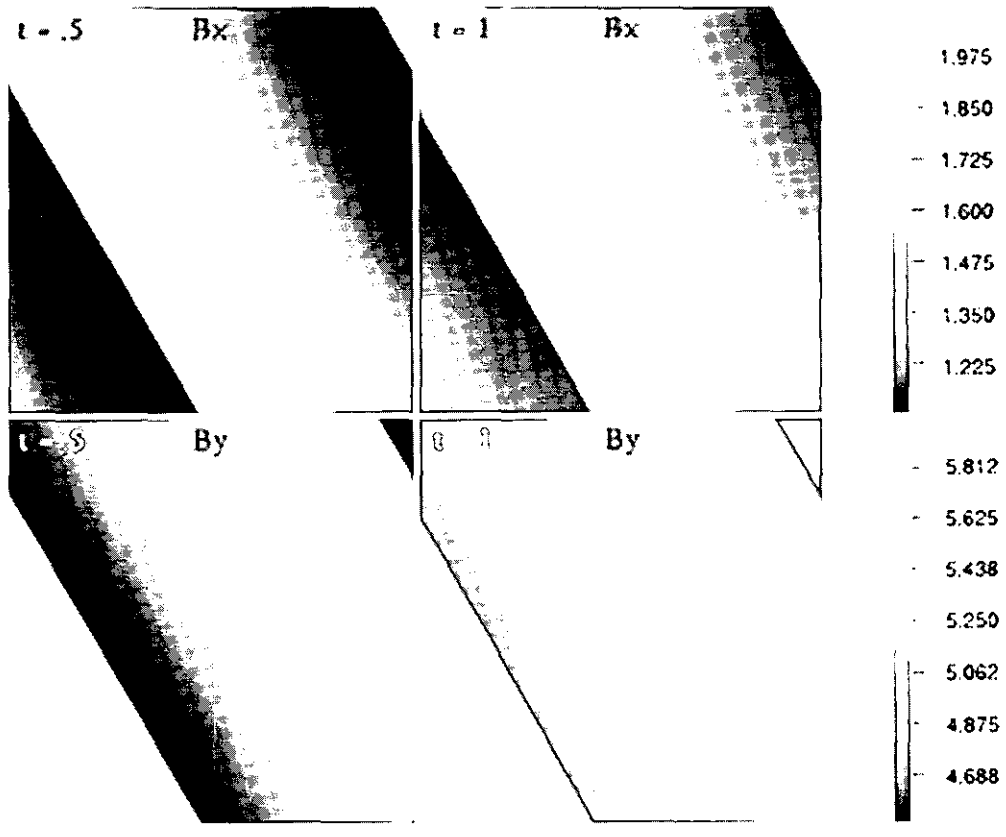

FIG. 16. A wave in a two-dimensional domain. The distributions of the two components of the magnetic field, B_x and B_y at $t = 0.5$ and $t = 1.0$.

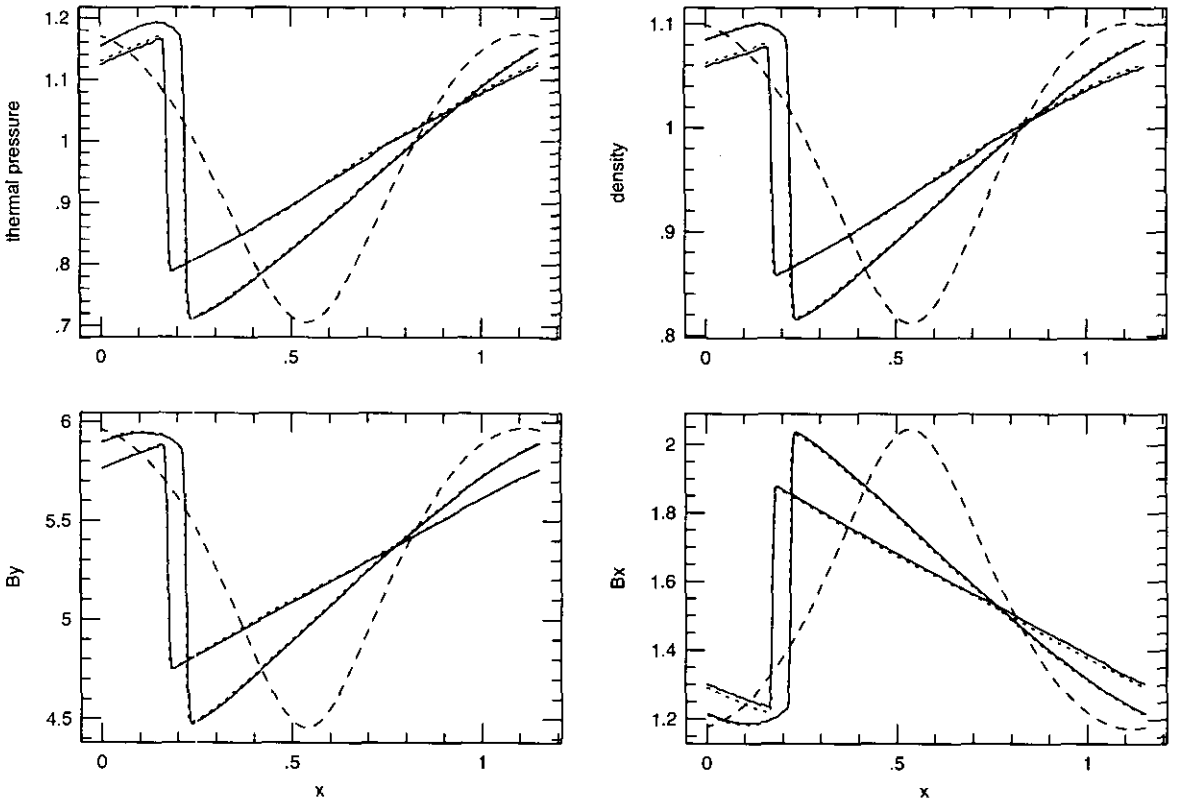

FIG. 17. The profiles along the line $y = 128$ zones at $t = 0$ (dashed), and at $t = 0.5$, 1.0 (solid) in the simulation for a fast wave in a two-dimensional domain. The dotted lines, which are hard to be seen, are the references obtained from our one-dimensional simulation at $t = 0.5$ and 1.0.

mance of our code for those MHD problems, we have applied our code to the interaction between MHD shocks and a cloud. In the remainder of this section, we will present the results from our simulation.

The simulation is performed on a 2×1 square with 512×256 uniform rectangular zones. The numerical model we have used is as follows. The x-axis is toward the direction of the shock propagation. The initial cloud is assumed to be a cylinder with a circular cross section. The z-axis is along the cylinder. Thus the y-axis is perpendicular to both the cylinder and the direction of the shock propagation. The shock front is initially located at $x = 1.2$. The center of the cross section of the cloud is initially located at $(x, y) = (1.4, 0.5)$ and the radius of the cross section is 0.18. The initial configuration of the problem is shown in Fig. 18. The reference is chosen such that the flow in the postshock state is at rest in our reference. Thus the flow in the preshock state moves toward the shock in this reference.

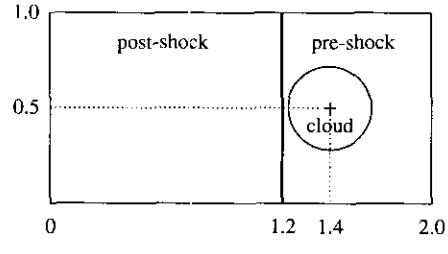

FIG. 18. The initial configuration for the interaction between a fast shock and a cloud.

The magnetic field components B_x and B_y are initially set to unity and zero, respectively, in the whole simulation domain. The initial preshock and postshock states for the fast shock are given by

$$\begin{bmatrix} \rho \\ p \\ u_x \\ u_y \\ u_z \\ B_z \end{bmatrix}_{\text{postshock}} = \begin{bmatrix} 3.88968 \\ 14.2614 \\ 0 \\ 0 \\ -0.05234 \\ 3.9353 \end{bmatrix}, \quad \begin{bmatrix} \rho \\ p \\ u_x \\ u_y \\ u_z \\ B_z \end{bmatrix}_{\text{preshock}} = \begin{bmatrix} 1 \\ 0.04 \\ -3.3156 \\ 0 \\ 0 \\ 1 \end{bmatrix}.$$

Thus the Mach number M ($\equiv W/C_{f0}$) = 10, or, $W/C_0 = 17.3$, where W is the shock speed with respect to the preshock state and C_{f0} and C_0 are the fast and sound wave speeds in the preshock state, respectively. The shock speed in the Eulerian coordinate is about 1.15. The initial cloud is five times more dense than the preshock state. The initial p, u_x, u_y, u_z, and B_z

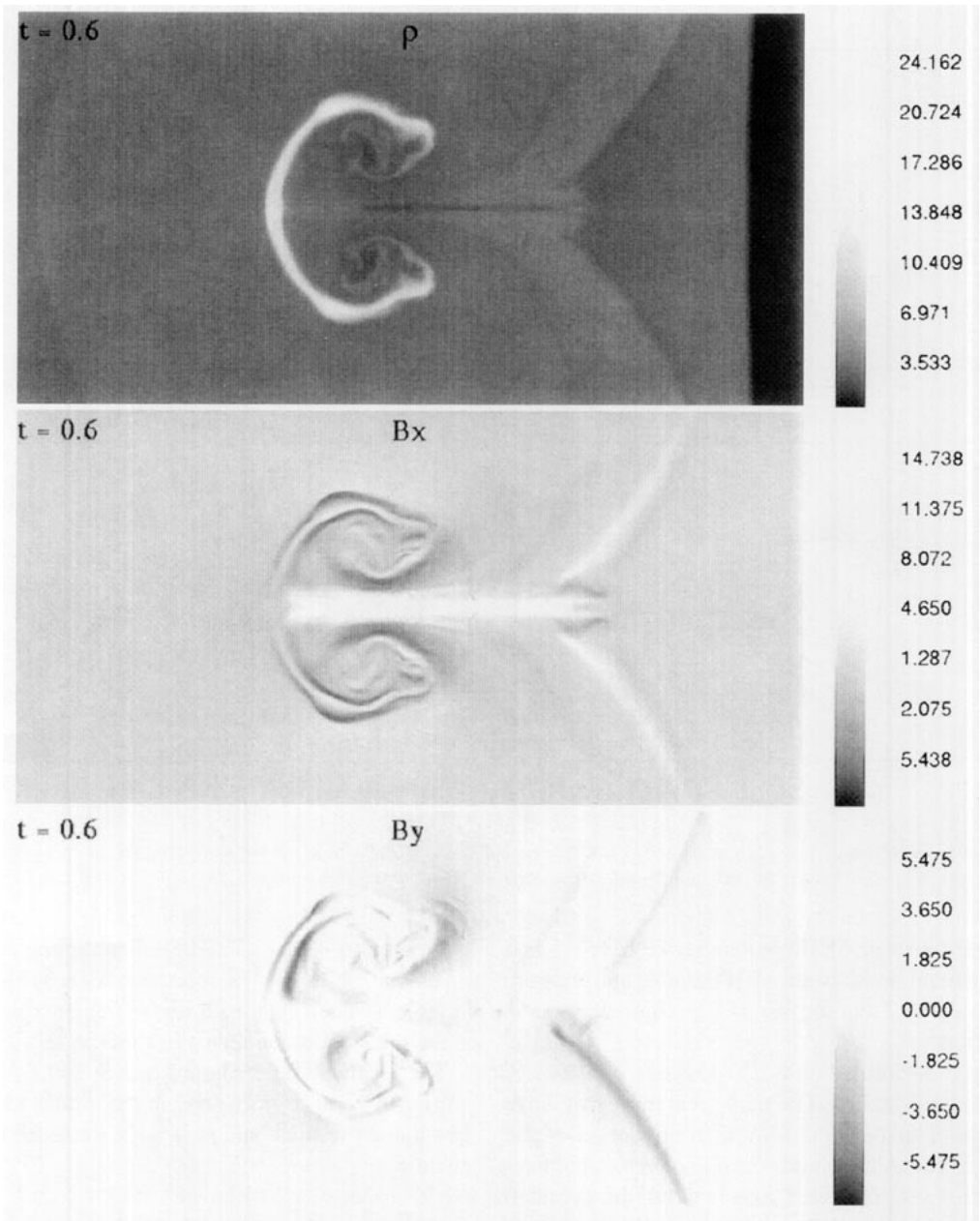

FIG. 19. The interaction between shocks and a cloud. The distributions for the mass density, two components of the magnetic field, B_x and B_y, at $t = 0.6$.

for the cloud are the same as in the preshock state. Under these initial conditions, the β (ratio between the thermal pressure and the magnetic pressure $\mathbf{B}^2/8\pi$) is about 0.5 in the preshock state, and it is about 21.7 in the postshock state. It is interesting to note that the thermal pressure is dominant over the magnetic field pressure in the postshock state, even though it is in the same order as the magnetic pressure in the preshock state.

Continuation boundary conditions are used. Our code actually simulates the lower half domain and the situation in the upper half domain is duplicated according to the symmetry about $y = 0.5$ plane. Figure 19 shows the distributions for the mass density, two components of the magnetic field, B_x and B_y, at $t = 0.6$.

5. CONCLUSIONS AND DISCUSSIONS

High-order Godunov schemes have been proven to be very effective for compressible gas dynamics. The main difficulties in the development of this type of scheme for MHD equations have been associated with the Riemann problem, the treatment of nonstrict hyperbolicity. A high-order Godunov scheme for multidimensional ideal MHD has been constructed based upon

TABLE VIIa

The Solutions for a Riemann Problem[a]

Regions	ρ	p	ux	uy	uz	By	Bz
L	1.000E + 00	1.000E + 00	0.000E + 00	0.000E + 00	0.000E + 00	3.545E + 00	1.000E − 08
R2	6.852E − 01	4.455E − 01	6.327E − 01	−2.151E − 01	−6.068E − 10	2.145E + 00	6.050E − 09
R3	6.852E − 01	4.455E − 01	6.327E − 01	−1.677E + 00	−6.656E − 08	−2.145E + 00	−1.875E − 07
R4	7.322E − 01	5.088E − 01	5.853E − 01	−1.575E + 00	−5.765E − 08	−1.900E + 00	−1.662E − 07
R5	2.345E − 01	5.088E − 01	5.853E − 01	−1.575E + 00	1.154E − 07	−1.900E + 00	−1.662E − 07
R6	1.167E − 01	8.690E − 02	−2.505E − 01	−1.743E − 01	2.379E − 07	−3.185E + 00	−2.784E − 07
R7	1.167E − 01	8.690E − 02	−2.505E − 01	−1.743E − 01	4.917E − 10	−3.185E + 00	8.983E − 09
R	1.250E − 01	1.000E − 01	0.000E + 00	0.000E + 00	0.000E + 00	−3.545E + 00	1.000E − 08

[a] $B_x = 2.65868$, $\gamma = 2$.

a nonlinear Riemann solver recently developed by the authors. The correctness of the scheme has been tested in the steepening of waves in one- and two-dimensional situations in various shock-tube problems which involve all the discontinuities in ideal MHD equations. The robust character of the scheme has been demonstrated through the problems mentioned above and through the interaction between MHD shocks and a cloud. From the results of these test problems, it appears that this extension of the PPM for gas dynamics to ideal MHD equations preserves the benefits which have been responsible for the success of the original scheme.

Although the scheme is for ideal MHD, its application is not restricted to ideal MHD. The scheme may be used for those MHD problems in which the internal structures of discontinuities are not important. For the MHD problems in which the physical dissipation terms are important, the physical dissipations may be incorporated by a separate step without changing the main part of the scheme.

It is clear from the description of the Riemann solver, if it is iterated to convergence, it requires a considerable amount of computation. Fortunately, a converged result is not required for the purpose of practical calculation. Extensive experience in the use of Riemann solvers of the type described here in the much simpler context of hydrodynamics has shown that more than a single nonlinear iteration of these Riemann solvers after the first is not required, even in the case of extremely strong shocks. Of course, in all but a handful of zones in a given strip from a given problem the initial guess which we have described in the latter part of Section 3.1 is all that is required. In the case of simple hydrodynamics, to aid vectorization of the code we perform a nonlinear iteration of the Riemann solver everywhere, whether or not it is needed. The cost of the unnecessary work in this case is minor. In MHD computations, however, we find that the cost of unnecessary nonlinear iterations of the Riemann solver is significant and should be removed by altering the code so that nonlinear iterations are performed only where they are needed. The cost of the nonlinear iterations is therefore problem dependent, to a small degree, and computer architecture dependent to a greater degree. Performance figures for the algorithm described above which we have obtained on a single Cray C90 processor executing vectorized code are as follows. It takes 16.1 CPU seconds to run 1000 time steps for a 1D problem with 1000 zones of computational grid, and it takes 232 CPU seconds to run 100 time steps for a 2D problem with 256×256 computational zones, using the nonlinear Riemann solver with a single iteration. Our current code implements the nonlinear Riemann solver for all the interfaces of zones, but we do anticipate a faster figure in a practical problem because the nonlinear iterations are required in a very small fraction of the zones of the computational grid. For some MHD problems, such as solar magneto-convection, the nonlinear iterations will not be required at all. The current computer codes remain to be improved and the most efficient implementation of the scheme remains to be found.

TABLE VIIb

The Convergence of Wave Speeds

Iterations	W_{f-}	W_{s-}	W_{s+}	W_{f+}
0	−1.5774E + 00	−5.4093E − 01	8.4216E − 02	4.1600E − 01
1	−1.3677E + 00	−4.4824E − 01	1.4373E − 01	4.1763E − 01

ACKNOWLEDGMENTS

We acknowledge useful discussions with Thomas W. Jones. We are grateful to the three referees for their comments and suggestions. This work was supported by the U.S. Department of Energy through Grant DEFG02-

REFERENCES

1. S. K. Godunov, *Math. Sb.* **47,** 271 (1959).
2. B. Van Leer, *J. Comput. Phys.* **23,** 276 (1977).
3. B. Van Leer, *J. Comput. Phys.* **32,** 101 (1979).
4. P. L. Roe, *J. Comput. Phys.* **43,** 358 (1981).
5. B. Engquist and S. Osher, *Math. Comput.* **36,** 321 (1981).
6. A. Harten, *J. Comput. Phys.* **49,** 359 (1983).
7. P. R. Woodward and P. Colella, *J. Comput. Phys.* **54,** 115 (1984).
8. P. Colella and P. R. Woodward, *J. Comput. Phys.* **54,** 174 (1984).
9. A. T. Giz, Ph.D. thesis, University of California, Berkeley, 1987.
10. A. T. Giz and P. R. Woodward, *Turkish J. Phys.* **16,** 353 (1992).
11. M. Brio and C. C. Wu, *J. Comput. Phys.* **75,** 400 (1988).
12. J. B. Bell, P. Colella, and J. A. Trangenstein, *J. Comput. Phys.* **82,** 362 (1989).
13. A. L. Zachary and P. Colella, *J. Comput. Phys.* **99,** 341 (1992).
14. A. L. Zachary, A. Malagoli, and P. Colella, *SIAM J. Sci. Stat. Comput.*, **15,** 263 (1994).
15. W. Dai and P. R. Woodward, *J. Comput. Phys.* **111,** 354 (1994).
16. M. Brio, in *Nonlinear Hyperbolic Equations—Theory, Computation Methods, and Applications: Proceedings, Second International Conference on Nonlinear Hyperbolic Problems, Aachen, FRG, March 14–18, 1988* (unpublished).
17. J. Glimm, in *Nonlinear Hyperbolic Equations—Theory, Computation Methods, and Applications: Proceedings, Second International Conference on Nonlinear Hyperbolic Problems, Aachen, FRG, March 14–18, 1988* (unpublished).
18. L. D. Landau and E. Lifshits, *Electrodynamics of Continuous Media* (Pergamon, New York, 1960).
19. R. Courant and K. O. Friedrichs, *Supersonic Flow and Shock Wave*, 5th ed. (Interscience, New York, 1967).
20. A. Jeffrey and T. Taniuti, *Non-linear Wave Propagation* (Academic Press, New York/London 1964).
21. A. G. Kulikovskiy and G. A. Lyubimov, *Magnetohydrodynamics* (Addison–Wesley, Reading, MA, 1965).
22. A. R. Kantrowitz and H. E. Petscheck, in *Plasma Physics in Theory and Application* (McGaw–Hill, New York, 1966).
23. P. R. Woodward, in preparation, 1994.
24. P. R. Woodward, in *Astrophysical Radiation Hydrodynamics*, edited by K.-H. A. Winkler and M. L. Norman (Reidel, Dordrecht, 1986).
25. G. Strang, *SIAM J. Numer. Anal.* **5,** 505 (1968).
26. G. Sod, *J. Comput. Phys.* **27,** 1 (1978).
27. R. DeBar, Lawrence Livermore National Laboratory Report UCIR-760, 1974 (unpublished).
28. J. U. Brackbill and D. C. Barnes, *J. Comput. Phys.* **35,** 426 (1980).